



A single wheel test rig for ocean world rovers

Athul Pradeepkumar Girija ^{a,*}, Rachana Agrawal ^a, Ye Lu ^a, Archit Arora ^a, Maxim de Jong ^b, Sarag J. Saikia ^a, James M. Longuski ^a

^a Purdue University, 701 W. Stadium Ave., West Lafayette, IN 47907, USA

^b Thin Red Line Aerospace, Chilliwack, British Columbia V2R 5M3, Canada



ARTICLE INFO

Article history:

Received 28 October 2022

Revised 2 June 2023

Accepted 4 July 2023

Keywords:

Planetary rover

Wheel

Test rig

Mobility system

Ocean worlds

ABSTRACT

Ocean Worlds such as Europa and Enceladus are known to harbor subsurface liquid water oceans under their icy crust and are high-priority targets for in situ exploration. Compared to the Moon and Mars, Ocean Worlds likely present significantly more challenging environment for surface mobility systems due to the extremely cold temperature, high radiation dosage, and poorly constrained material properties under these conditions. Small-diameter wheels such as those used by Mars rovers are prone to slip-sinkage in loose soil and damage from sharp rock and ice formations. A 4-wheel rover with a simple drive system and large deployable compliant tires is proposed as a solution for extreme terrain mobility on Ocean World surfaces. The present work describes the design and construction of a single wheel test rig and a prototype large-diameter deployable wheel for Ocean World rovers and initial test results. The test rig allows independent control of the vertical load, slip ratio, slip angle, and camber angle, and accommodates large-diameter deployable wheels. The test rig features a modular test bed that can simulate varied surface features such as fine-grained ice, smooth hard ice, sharp ice formations, and large ice boulder fields.

© 2023 ISTVS. Published by Elsevier Ltd. All rights reserved.

1. Introduction

Mobility systems have provided immense value for in situ planetary exploration over the last five decades since Lunokhod-1, the first successful robotic rover to operate on the lunar surface in 1970 (Sanguino, 2017; Kassel, 1971). Compared to orbital platforms which can only perform remote-sensing investigations and static landers which provide in situ data but only for a single site, mobility systems enable in situ measurements across a range of scientifically interesting sites. A wide range of mobility systems have been proposed for planetary exploration across the Solar System, including rovers (Iagnemma and Dubowsky, 2004), articulated robots (Preumont et al., 1997), hoppers (Fiorini et al., 1999), helicopters (Balaram et al., 2018), multicopters (Hassanalian et al., 2018; Barnes et al., 2021), airplanes (Landis et al., 2005), balloons and airships (Yajima et al., 2009), ice drills (Weiss et al., 2008), boats (Mitri et al., 2014; Lorenz et al., 2018), and submersibles (Oleson et al., 2018). At the time of writing, NASA's Curiosity and Perseverance rovers and Chinese National Space Agency's (CNSA) Zhurong rover are operational on the Martian surface (Welch et al., 2013; Williford et al., 2020; Tian et al.,

2021). CNSA's Yutu 2 lunar rover has been operational for over 3 years and has become the longest operational lunar rover, breaking Lunokhod-1's previous record of 10.5 months (Ling et al., 2019). The continued interest and commitment in surface mobility systems, despite their inherently higher costs compared to orbiter and lander missions, underscore their importance in future planetary exploration. However, the poorly known surface properties and features (such as loose sand, boulder fields, sharp rock, and ice) present significant engineering challenges to surface mobility systems. The most notable example is NASA's Spirit rover which became trapped in soft sand and could not gain traction to free itself, eventually leading to the loss of the mission (Lorenz and Zimbelman, 2014). Prior to the embedding event, the Spirit rover had experienced significant slippage when crossing fine-grained surfaces (Li et al., 2008). The twin rover Opportunity has also been a subject to such near-embedding events as it traversed deformable sand terrain (Zhou et al., 2014; Arvidson et al., 2021). Similar slippage and sinkage problems were encountered by the Curiosity rover when crossing ripple fields (Arvidson, 2014); in addition to significant wheel damage from traversing over sharp rock outcrops (Arvidson et al., 2017). These experiences underscore the importance of wheel-soil/terrain interaction for future rover missions. The Mars rovers used a combination of numerical modeling, single-wheel test rig experiments, and full vehicle field tests in

* Corresponding author.

E-mail address: apradee@purdue.edu (A.P. Girija).

analog sites such as the Mojave Desert to characterize the wheel-terrain interaction. Based on the models and experimental data, the operations teams select the best possible path so as to minimize the risk of events such as embedding in a sand trap, or plan a recovery path in case of such an event.

While the majority of the existing literature in the field of planetary rovers focus on the Moon and Mars, the Ocean Worlds such as Europa and Enceladus in the outer Solar System are high-priority targets for in situ exploration in the near future (Sherwood et al., 2018). These Ocean Worlds are known to harbor massive liquid water oceans underneath their icy crust and are prime candidates in the search for life beyond Earth (Nimmo and Pappalardo, 2016; Lunine, 2017). Multiple studies have investigated the scientific potential (Pappalardo et al., 2013; Patthoff et al., 2018; Hand et al., 2017), mission architecture (Hand et al., 2022), and technical challenges of lander and mobile platforms on Europa and Enceladus (Hobley et al., 2013; Nayar et al., 2017). Ocean Worlds such as Europa present a significantly more challenging environment compared to Mars due to the extremely cold temperature, high radiation dosage, and poorly constrained material properties under these conditions (Marteau, 2021). Preliminary studies using photopolarimetric observations suggest that granular ice under cryogenic and vacuum conditions may be extremely fine-grained material and thus a potential hazard to landed spacecraft (Nelson et al., 2018). Other potential hazards include penitent-like formations which create sharp ice outcrops (Hobley et al., 2018), and massive boulder fields as seen by Cassini during close flybys of Enceladus (Porco et al., 2006). The present work details the design of a unique single wheel test rig at Purdue University to characterize wheel terrain interactions for future Ocean World mobility systems. The work also presents a novel deployable large-diameter wheel that is particularly suited for overcoming large obstacles such as boulder fields. The test rig accommodates tires that can deploy to diameters as large as 2 meters from a stowed configuration, and features a modular test bed that can simulate varied surface features such as fine-grained ice, smooth hard ice, sharp rock formations, and boulder fields. This paper reports the design, construction, capabilities, and initial test results of the test rig with the prototype deployable wheel.

2. Existing single wheel test rigs for planetary rovers

Understanding wheel-terrain interaction requires a combination of theoretical methods, numerical models, and experimental techniques. A single wheel test rig is often used to validate the terramechanics models as well as provide empirical relationships for use in these models. Numerous single wheel test rigs have been developed by universities and other institutes to characterize wheel-terrain interaction in support of planetary missions. This section provides a brief overview of a selected set of existing single wheel test rigs and their capabilities. Fig. 1(a) shows the Massachusetts Institute of Technology (MIT) single wheel test rig used in support of the testing for the Curiosity rover operations on the Martian surface (Senatore et al., 2014). The test rig allows control of the wheel slip ratio and the vertical load and measures the traction force, driving torque, and wheel sinkage in Mars simulant soil. Fig. 1(b) shows the Carnegie Mellon University (CMU) single wheel soil imaging test bed also used in support of the Curiosity rover (Moreland et al., 2012). The CMU test rig provides a unique imaging analysis capability of soil motion at and below the wheel-soil interface. Fig. 1(c) shows the Rover Chassis Evaluation Tool (RCET) single wheel test rig built at the German Aerospace Center (DLR) in support of the ExoMars rover project (Gallina et al., 2014). Fig. 1(d) shows the single wheel test bed at Tohoku University designed to support Japanese lunar exploration missions (Ishigami et al., 2007).

In addition to the vertical load and slip ratio, the test rig allows control of the slip angle for the experiments. Fig. 1(e) shows the single wheel test rig at Politecnico di Torino built to support the AMALIA lunar rover mission and features slip and camber angle control during the test (Genta and Pizzamiglio, 2016). Fig. 1(f) shows the wheel-soil interaction test bed at Harbin Institute of Technology (HIT) in support of Chinese lunar exploration program (Ding et al., 2011). Table 1 summarizes the key characteristics and test capabilities of the various single wheel test rigs described in this section, and are compared to the Purdue University single wheel test rig for Ocean World rovers. More extensive reviews of both computational and experimental techniques for planetary wheel-soil interaction are available in the literature (Ding et al., 2013; Schäfer et al., 2010; Sreenivasulu and Jayalekshmi, 2014).

3. Design and fabrication of the single wheel test rig

The high-level objectives of the work described in this paper are as follows: 1) Design and construction of a single wheel test rig for Ocean World rovers, 2) Construction of a prototype novel large-diameter deployable rover wheel, and 3) Demonstrate the test rig capabilities using the prototype wheel under a range of slip ratios and surface conditions expected on Ocean World surfaces. The focus of the effort is on the wheel-terrain interaction of the large wheel with various simulated surface features that may be found on Ocean Worlds. The tests do not, however, directly simulate the cryogenic temperature, high radiation, and high vacuum, and all the tests are done in room temperature conditions. The requirements for the test rig are derived from these high-level objectives and are described in the following subsections. Section 4 provides a detailed description of the design, fabrication, and design rationale of the prototype wheel.

3.1. System requirements and constraints

The overall rig design is driven by the requirement to accommodate the prototype wheel which is approximately 1 meter in diameter and 25 cm in width. During the early stage of the design, the choice between using a horizontally moving surface with the wheel held in place was considered, as opposed to a static surface on which the wheel will be rolled over. While a moving underlying surface is ideally suited for flat surfaces and is widely used in the automobile industry for dynamic wheel testing, it presents inherent difficulties when flexibility is required in terms of the nature of the surface. To accommodate a wide range of surface features such as granular ice and boulder fields, it was decided to use a horizontally moving wheel over a static test bed which can be easily reconfigured with different surface conditions during the test. The length of the test rig is driven by the requirement for a 1 meter diameter tire to complete at least full rotation during a test which requires 3.14 m of test bed length with an additional 20% margin added to accommodate transient motion during start of the test when the wheel is reaching the desired slip condition. This imposed a requirement of at least 3.8 meters of usable test bed length. The maximum allowable length (due to space constraints) of the test rig is 6.0 meters. Considering these constraints, the available volume for the test rig is 6 m × 2 m × 2 m (length × width × height), which provides approximately 4.5 meters of usable test bed length. The next major requirement is to be able to test the prototype wheel under a range of slip ratios to characterize traction and wheel sinkage. The wheel slip ratio s is a non-dimensional parameter defined as follows (Ishigami et al., 2007).

$$s = \begin{cases} (r\omega - v_x)/r\omega & \text{if } |r\omega| > v_x, \text{ positiveslip} \\ (r\omega - v_x)/v_x & \text{if } |r\omega| < v_x, \text{ negativeslip} \end{cases} \quad (1)$$

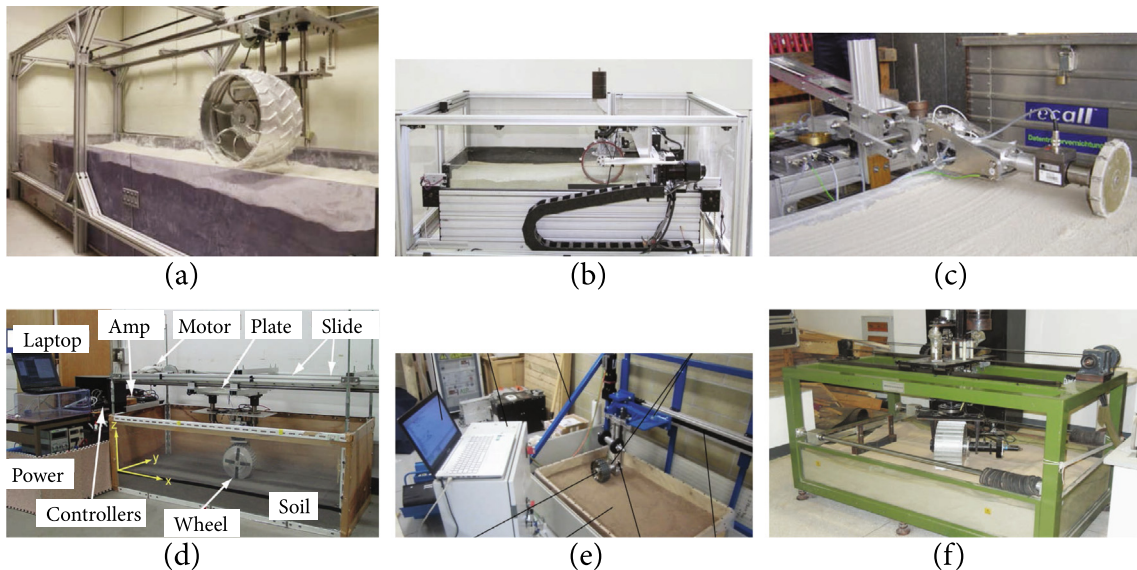


Fig. 1. Various existing planetary rover single-wheel test rigs. (a) MIT Single Wheel Test Rig (Senatore et al., 2014); (b) CMU Single Wheel Soil Imaging Testbed (Moreland et al., 2012); (c) DLR ExoMars Project Single Wheel Test Rig (Gallina et al., 2014); (d) Tohoku University Single Wheel Test Bed (Ishigami et al., 2007); (e) Politecnico di Torino Single Wheel Test Rig (Genta and Pizzamiglio, 2016); (f) HIT Wheel-Soil Interaction Test Bed (Ding et al., 2011).

Table 1
Summary of key characteristics and capabilities of the various single wheel test rigs.

	Length, m	Speed, cm/s	Tire diameter, cm	Slip ratio control	Slip angle control	Camber angle control	Dynamic load control
MIT(Senatore et al., 2014)	3.5	6	50	✓	✗	✗	✗
CMU(Moreland et al., 2012)	1.0 ^a	2	50	✓	✗	✗	✗
DLR(Gallina et al., 2014)	3.0 ^a	n/a ^b	25	✓	n/a ^b	n/a ^b	✗
Tohoku(Ishigami et al., 2007)	2.0	3.5	20	✓	✓	✗	✗
Torino(Genta and Pizzamiglio, 2016)	2.7	n/a ^b	18	✓	✓	✓	✗
HIT(Ding et al., 2011)	1.7	n/a ^b	40	✓	✓	✗	✗
Purdue	4.8	20	200	✓	✓	✓	✓

^a Estimated by the authors.

^b Data not available.

where r is the wheel radius, ω is the wheel angular speed, and v_x is the horizontal traverse speed. A desired slip ratio is achieved by independently controlling both the wheel angular speed and the horizontal traverse speed. Planetary rovers typically operate at very low speeds (< 10 cm/s), and hence most existing single wheel test rigs are designed to operate at such speeds as seen in Table 1. For example, the Curiosity rover has a maximum operating speed of 4 cm/s on flat ground (Ellery, 2016). The Purdue University test rig can accommodate traverse speeds as high as 20 cm/s, which may be feasible for future rovers. Fig. 2 shows the required angular speed as a function of the horizontal speed for a range of slip ratios. Ideally, it would be desirable for the test rig to be capable of accommodating a wide range range of slip ratios ($[-1, +1]$). However, as seen in Fig. 2, this is not practical as the required angular velocity increases sharply as the slip ratio approaches 1.0. Due to constraints on the wheel drive motor's achievable RPM, the angular speed is limited to 1 rad/s. Considering these constraints, the selected operating range for ω and v_x is shown in green in Fig. 2 which allows slip ratios as high as 0.8 for a traverse speed of 0.1 m/s.

The vertical load on the wheel F_z is another important test parameter and must be controlled to simulate the wheel-surface interaction on planetary surfaces with different values of surface gravity. The prototype test wheel is intended to be used on a 4-wheel rover weighing approximately 800 kg which will be delivered to Europa's surface using an MSL-derived sky-crane descent

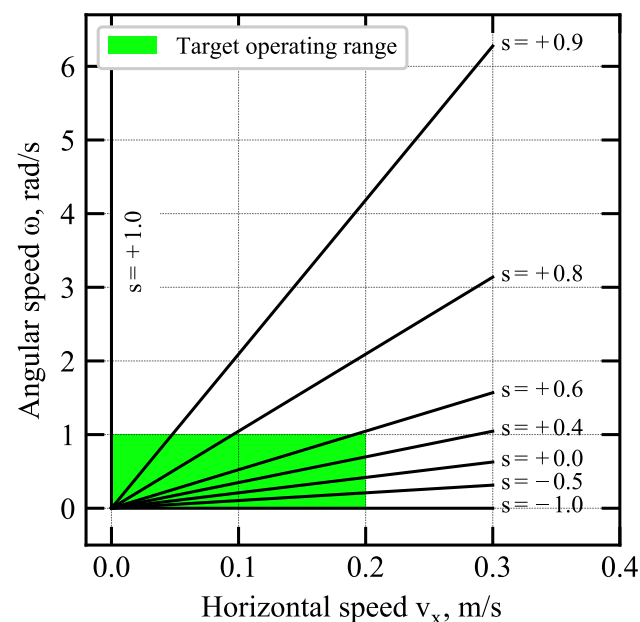


Fig. 2. Required wheel angular speed as a function of horizontal traverse speed at various slip ratios (for the prototype test wheel with diameter = 0.956 m).

system as shown in Fig. 3. Taking into account Europa's surface gravity of 1.32 m/s^2 , this results in a vertical load of 264 N for each wheel. The corresponding loads on Mars, Titan, and Enceladus are 744 N, 270 N, and 22 N respectively. If the vehicle is moving up or down a slope, the local vertical component of the force will be smaller as defined by the slope angle. Considering these loads, the requirement for the vertical load on the wheel is in the range of 20–400 N. The nominal load accuracy requirement is arbitrarily set to 1% of the desired value, though this is not practical at very low vertical loads (i.e., < 20 N). The requirements for slip angle α and camber angle β (as illustrated in Fig. 4) are both arbitrarily defined at ± 25 degrees, which is comparable with other existing test rigs (Ishigami et al., 2007; Genta and Pizzamiglio, 2016) and a nominal upper bound for the range of these angles expected for planetary rovers under normal steering conditions (Ishigami, 2008).

The testbed needs to accommodate the prototype 25-cm wide wheel in the slip and camber angle geometries and is required to be at least 70 cm wide and 30 cm deep. The testbed is required to be able to simulate a wide range of conditions that may be expected on icy moons such as Europa. Fig. 5 shows some of the highest-resolution photographs of Europa and Enceladus from the Galileo and Cassini-Huygens spacecraft. A lander would be less than a pixel wide in even the highest resolution images of Europa, and terrain roughness at the lander scale will remain unknown until the Europa Clipper mission obtains higher resolution images of Europa's surface. The material properties of ice under such conditions are also not well understood. Laboratory studies using observational data from spacecraft and telescopes, as well as experimental studies of water ice under cryogenic and vacuum conditions, are currently underway at various facilities (Henderson et al., 2019; Potter et al., 2020). As a starting point, the test bed is required to be able to accommodate granular ice simulant, boulder fields, and sharp ice formations and also provide a flat hard surface resembling smooth ice (Reid et al., 2020). Analog sites such as the ones shown in Fig. 6 may offer some insight into

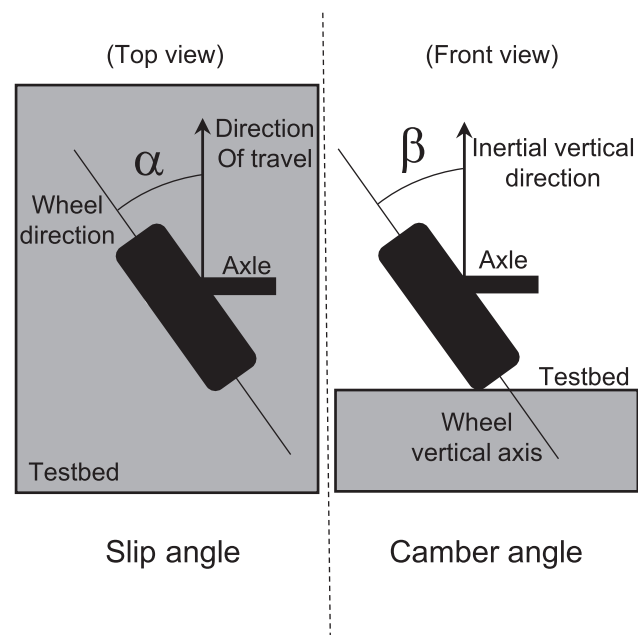


Fig. 4. Schematic illustrating slip and camber angles.

the conditions on these icy worlds, though ice is known to behave very differently under cryogenic conditions than that encountered on Earth. As more data becomes available, other test bed simulants and surface features may be used to provide a more realistic representation of surfaces.

The most important measurements of interest are the forces and moments on the wheel as it rolls across the surface under different test conditions, and is accomplished using a 6-axis Force Torque (FT) sensor. Fig. 7 shows the wheel coordinate system centered at the wheel hub and the definition of the drawbar pull F_x ,

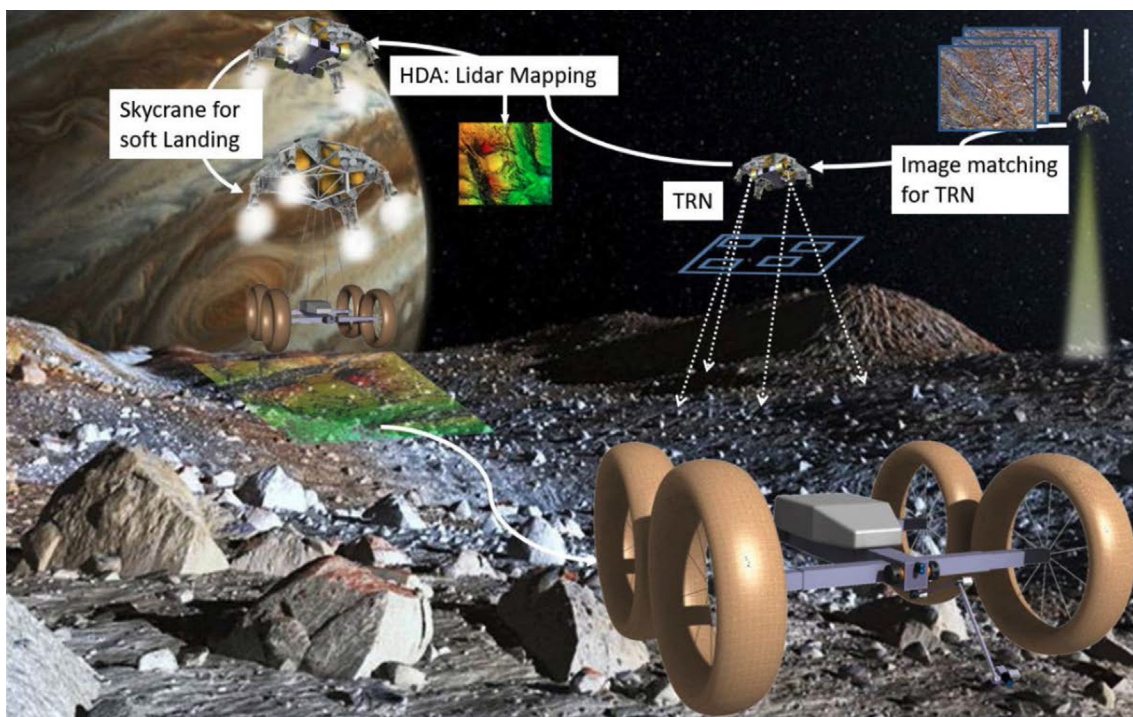


Fig. 3. Nominal mission concept of operations for the 4-wheel rover with larger diameter wheels landing at Europa on an MSL-derived skycrane system.

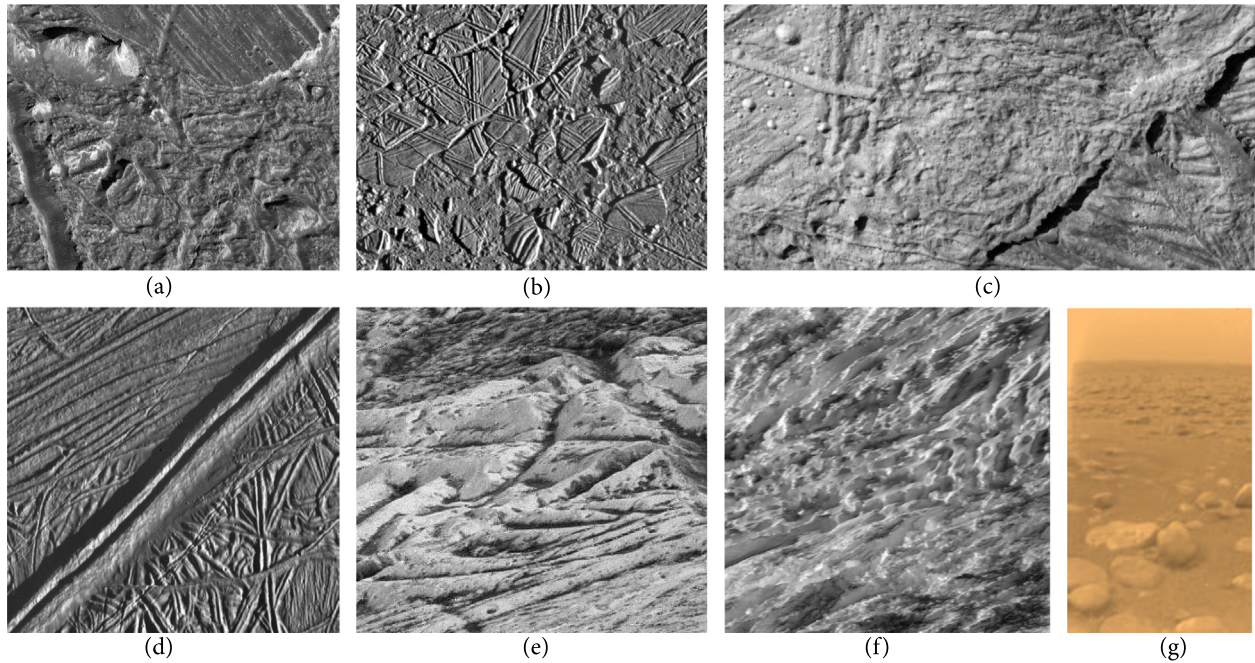


Fig. 5. High-resolution spacecraft images of various Ocean Worlds. (a) View of the Conamara Chaos on Europa. The image is 5 km wide (NASA/JPL/PIA01177). (b) High-resolution image of Europa's jumbled crustal plates, showing an area 42 km wide (NASA/JPL/PIA00591). (c) High-resolution image of Europa's surface showing numerous impact craters amid rugged terrain, image is 8 km wide (NASA/JPL/PIA01404). (d) Close-up image of one of Europa's ubiquitous double ridges. The double ridge is 2.6 km wide and rises to about 300 m. (NASA/JPL/PIA00589). (e) Highest resolution image of Europa showing an area 1.8 km wide (NASA/JPL/PIA01180). (f) Close-up view of Enceladus, showing an area 7.6 km wide (NASA/JPL/PIA17204). (g) Titan's surface as seen by the Huygens probe showing pebble-sized ice blocks about 15 cm across (ESA/NASA/JPL/PIA07232).

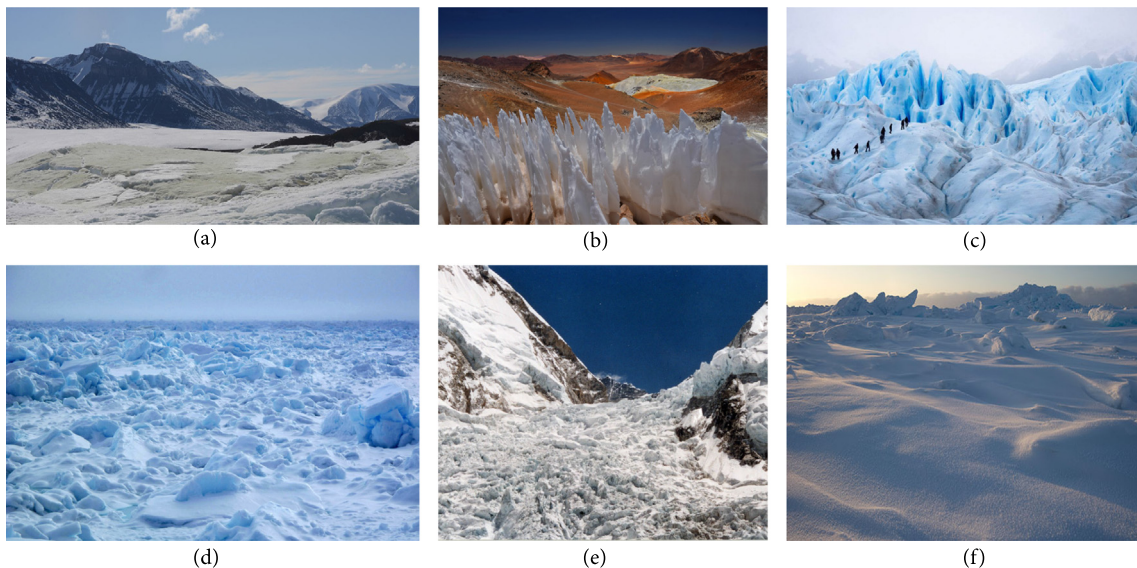


Fig. 6. Various ice formations on Earth, some of which may be representative of the landscapes on icy moons such as Europa and Enceladus. (a) Sulfidic outcrop (yellow colored marking on the ice) in Borup Fiord Pass glacier, Ellesmere Island in the Canadian High Arctic (NASA/John Spear at the Colorado School of Mines). (b) Penitentes on the Cerro Toco volcano in the Atacama Desert in Chile. Penitentes have been discovered on Pluto (Moore et al., 2017), and may be present at Europa at some latitudes (Hobley et al., 2018). Credit: Federico Ce. (c) Extremely rugged ice formations in the Perito Moreno Glacier in Argentina, note the people for scale. Such terrain is likely present on icy moons and presents formidable challenges for mobility systems. Credit: www.macdermottsaargentina.com. (d) Sea ice floating off the coast north of Barrow, Alaska. Credit: Ned Rozell/University of Alaska, Fairbanks. (e) Jumbled up ice blocks each several tens of meters to a few meters in size at the Khumbu Icfall in Nepal en route to Mt. Everest. Credit: Uwe Gille, Wikipedia, CC-BY-SA-3.0. (f) Powdery snow on sea ice near Barrow, Alaska. Credit: Chris Linder/University of Washington. Such terrain is likely present at Enceladus' south polar regions from freshly fallen material ejected from the active geysers (Porco et al., 2006) and may present a hazard for landers and rovers which may sink into the surface.

lateral force F_Y , normal force F_Z , lateral rolling moment M_X , drive torque M_Y , and the aligning torque M_Z . Wheel displacement in the vertical direction is required to measure sinkage, and along the horizontal direction to measure wheel slippage. A LabVIEW

program is developed to set the various test parameters (horizontal traverse speed, wheel rotational speed, vertical load, slip angle, camber angle) and record the measurements (wheel forces and torques, vertical and horizontal displacement) during the test.

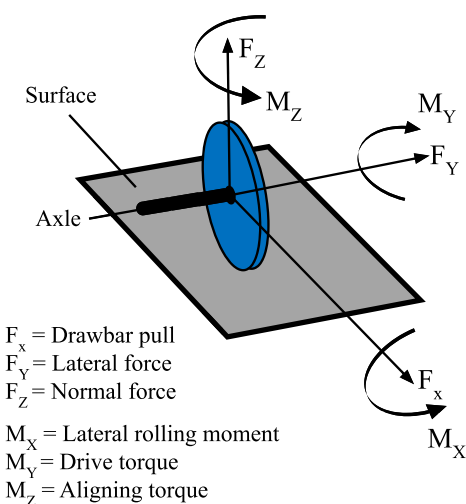


Fig. 7. Wheel forces and moments.

3.2. Mechanical system design

The test rig mechanical system consists of the following subsystems as shown in Fig. 8: main structure, horizontal motion control, vertical motion and load control, slip and camber angle control, wheel drive, and simulant bed. Details of each of the subsystems and their construction are given below.

3.2.1. Main structure and horizontal motion control

The main structure is made of standard slotted aluminum extrusions and is 6 meters long, 2 meters wide, and 2 meters high as shown in Fig. 9(a). Horizontal motion control is achieved using a carriage supported on wheels as shown in Fig. 9(b). The carriage is the primary moving structure and supports the various subsystems below including the vertical load control and the wheel drive mechanism, all of which move along with the carriage. The carriage is driven using a pulley and timing belt, which is connected to a motor as seen in Fig. 9(c). The top of the frame serves as a

guide rail for the carriage as it moves horizontally. By controlling the speed of the drive motor, the horizontal traverse speed of the wheel can be set to the desired value.

3.2.2. Vertical motion and load control

The main goal of the vertical motion and load control system is to control vertical force on the wheel, particularly to offload some weight to simulate its motion in reduced-gravity environments such as those encountered on Europa and Enceladus. The entire wheel assembly is supported on rollers as shown in Fig. 10(a) and 10(b), and can move in the vertical direction. The load control is achieved using a linear actuator and an extension spring. The linear actuator controls the tension on the spring and hence changes the forces transmitted to the wheel by the system weight. The desired vertical load is set by a feedback-loop control of the length of the extension spring using the linear actuator. A single-axis load cell as shown in Fig. 10(c), is used to measure the vertical load on the wheel continuously during the test and adjust the spring extension.

3.2.3. Slip and camber angle control

The slip and camber angle control system allows setting desired slip and camber angles at the beginning of a test. The range of achievable angles is $\pm 30^\circ$ for both slip and camber, which fulfills the requirement of at least $\pm 25^\circ$ angle. Slip and camber control is achieved using a linear actuator and a gear motor as shown in Fig. 10(a). The slip mechanism consists of a linear actuator that changes the angular position (i.e., slip angle) of the wheel-motor assembly arm. The actuator extends out to rotate the wheel counter-clockwise about the vertical axis (Z-axis) as shown in Fig. 10(a). A rotary sensor attached to the hinge measures the slip angle about the axis of rotation. The camber mechanism consists of a servo motor-gear system that can move the wheel-motor assembly about the traverse axis (X-axis). An inclinometer attached to the wheel-motor assembly rod measures the camber angle. Fig. 11(c,d) illustrates the slip and camber angle control systems in use during tests. The current systems only allow static slip and camber angle testing, since testing with dynamic slip and camber angle requires a constant contact patch between the wheel and surface which are more complicated to implement and will require more degrees of freedom on the wheel motor assembly.

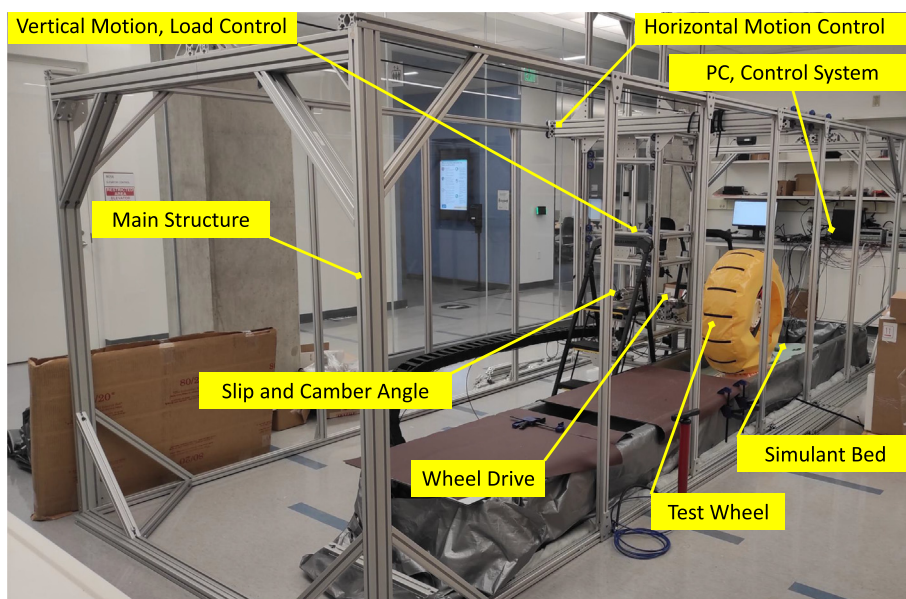


Fig. 8. Key elements of the Purdue single wheel test rig for Ocean World rovers.

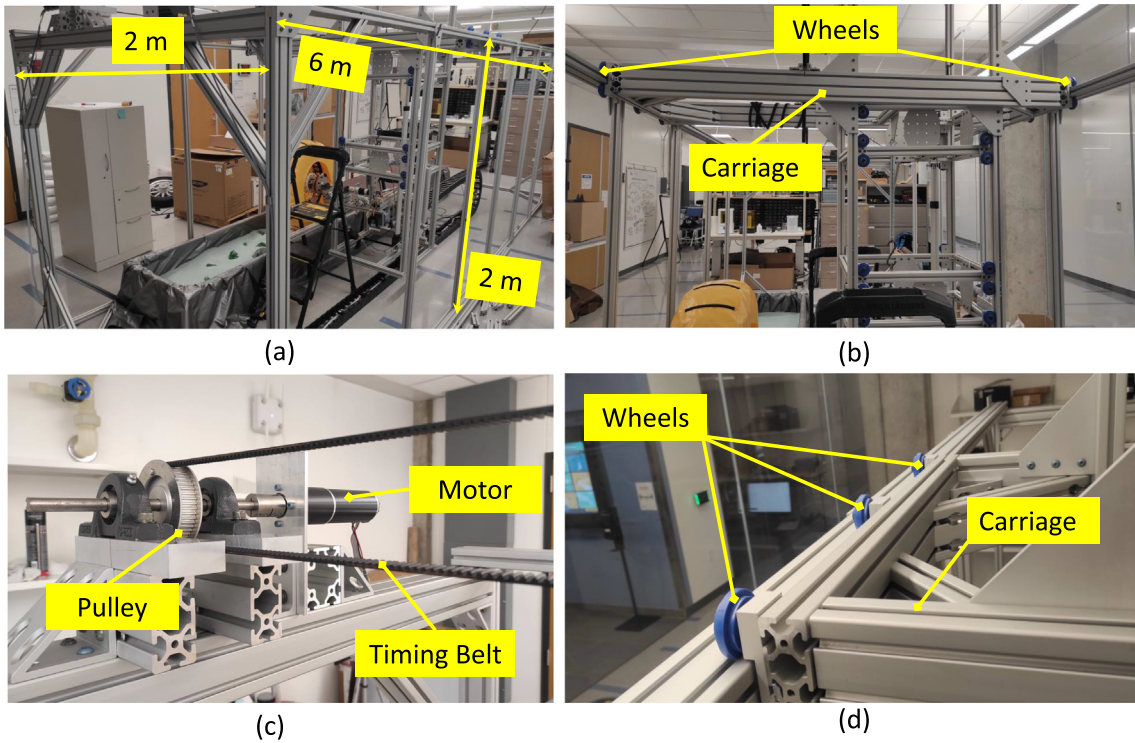


Fig. 9. (a) Dimensions of the main structure. (b) Carriage for horizontal motion, and carriage wheels that move along the main structure. (c) Carriage drive system using a pulley, timing belt, and drive motor. (d) Close-up view of carriage wheels on the guide rails.

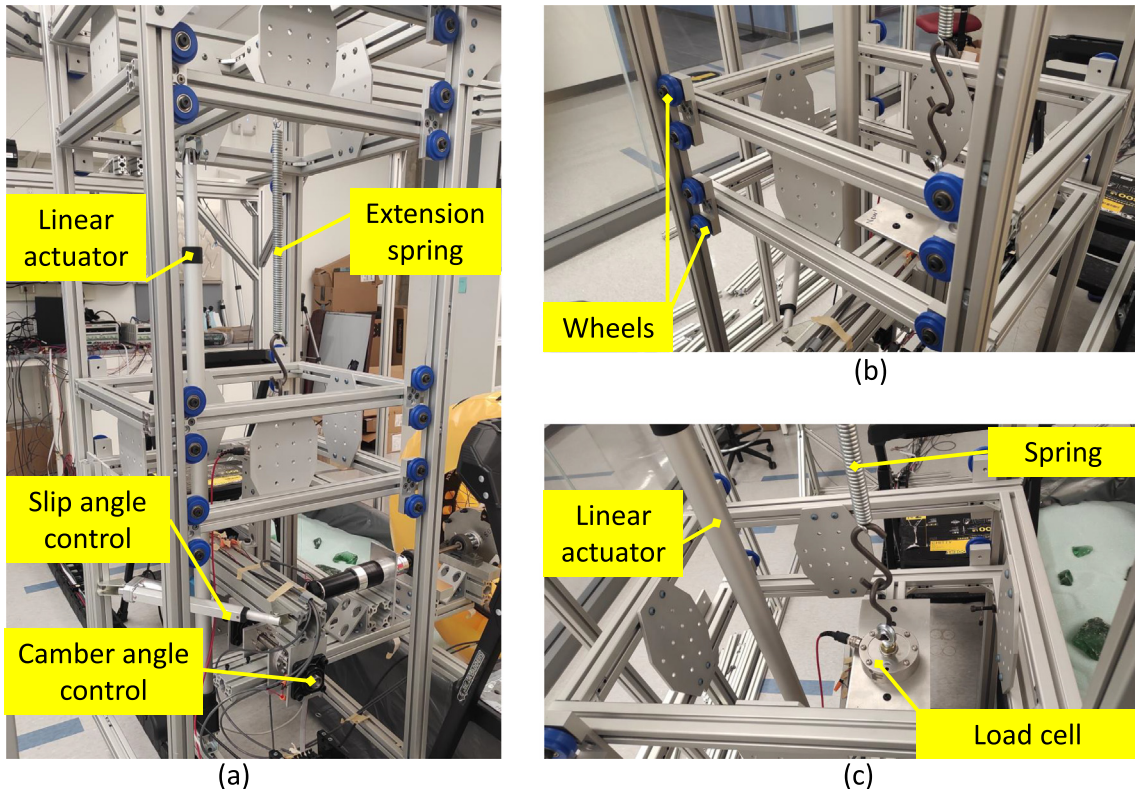


Fig. 10. (a) Linear actuator and extension spring used for vertical load control. (b) Rollers for vertical motion. (c) Load cell for measuring the vertical force on the wheel.

3.2.4. Wheel drive

The test wheel is driven using a DC motor as shown in Fig. 11(a). A six-axis force and torque (FT) sensor is mounted between the test

wheel and the mounting adapter plate to measure the reaction force and torque. Fig. 11(b) shows the assembled wheel motor drive with zero slip and zero camber angle. Fig. 11(c) shows the

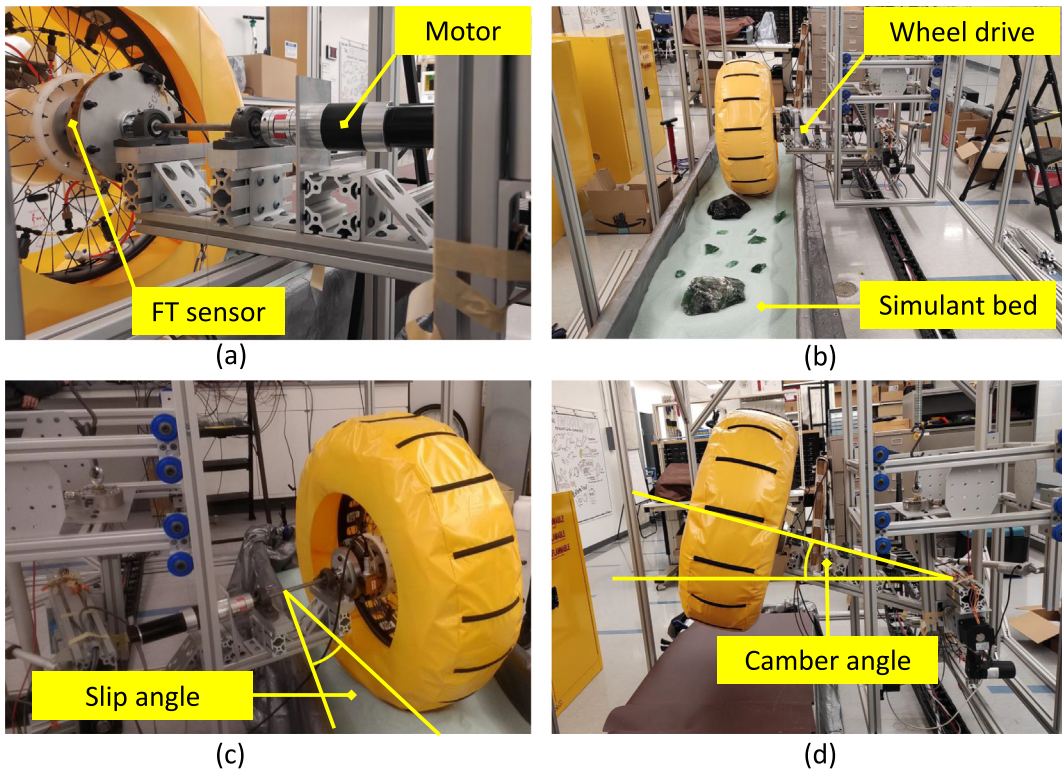


Fig. 11. (a) Drive motor and FT-sensor placement. (b) Zero slip and zero camber angle. (c) Non-zero slip angle and zero camber. (d) Zero slip angle and a non-zero camber.

wheel at a non-zero slip angle and zero camber angle during a test. Fig. 11(d) shows the wheel at zero slip angle and a non-zero camber angle.

3.2.5. Simulant bed

The simulant test bed is designed to be modular and easily reconfigurable to accommodate a wide range of surface conditions which may be present on Ocean World surfaces. Fig. 12(a) shows a flat rough surface created using sandpaper laid on top of a polycarbonate panel. Fig. 12(b) shows a flat smooth surface to simulate smooth ice created using a polycarbonate panel. Fig. 12(c) shows the tire on a snow simulant created using fine glass bubbles. Fig. 12(d) shows the tire in a simulated snow and ice boulder field (irregular shaped glass blocks with sharp edges) which is most likely the kind of terrain a rover will encounter. However, in the absence of additional data from a future mission it is not possible to predict if any of the surface conditions listed here will match the real environment at a particular landing site. Hence, it is only possible to simulate a wide range of surface conditions that may be present.

3.3. Electrical and control system design

Fig. 13 shows electrical and control system layout of the test rig. The test rig sensors include the FT sensor, vertical load sensor, slip and camber angle sensor, horizontal and vertical draw-wire sensors. The actuators include the wheel drive motor, vertical load control actuator, slip and camber actuators, and the carriage drive motor. Fig. 14 shows the motor controller and sensor data acquisition setup. The motors are controlled through individual motor controllers that receive command from the computer through a LabVIEW interface. The sensors send the signal to the PC through the National Instrument data acquisition input/output device. All instruments are powered through two DC power supplies. The motors, actuators, and sensors, including wheel motor, slip and

camber actuators and the FT sensors, are attached to the moving carriage frame and moves back and forth along with the carriage. The wiring and cables from instruments on the carriage are routed through an energy chain as shown in Fig. 15 to allow smooth movement of the cables wiring along length of the test rig as the carriage moves back and forth during a test run.

3.3.1. Actuators

The test rig uses a total of five actuators: three motors one each for horizontal carriage motion, wheel drive, and camber mechanism; and two linear actuators for vertical load control and slip angle mechanism. The carriage motor and wheel motor are both 200 Watt Maxon RE 50 DC motors. The carriage drive motor is paired with Maxon GP 52C gear which provides a reduction ratio of 126:1, and the wheel drive motor is paired with Maxon GP 62A with a reduction ratio of 236:1. The camber motor supports the entire wheel drive assembly as shown in Fig. 11d) and requires high torque to actuate the long drive arm. A high torque GBPH-0902-NP-100 Anaheim Automation stepper motor which provides a reduction of 100:1 is used to control the camber angle. The linear actuator for the load control is a Progressive Automation PA-04 capable of a maximum stroke length of 1 m and a maximum dynamic load of 1800 N. For slip angle control, the Progressive Automation PA-14 linear actuator is used with a stroke length of 0.2 m which allows slip angles from 0 to 30 degrees.

3.3.2. Sensors

The six-axis force and torque sensor is the primary sensor of the test rig which measures the three-axis forces and torques on the wheel. Based on the expected forces and torques on the wheel, the selected FT sensor is the ATI Omega-160 (DAQ version) with a maximum measurable single-axis force of 6250 N and 2500 N along axial and longitudinal directions respectively, and maximum measurable single-axis torque of 400 N·m in each axis. A single-axis load cell is used to measure the vertical load and achieve

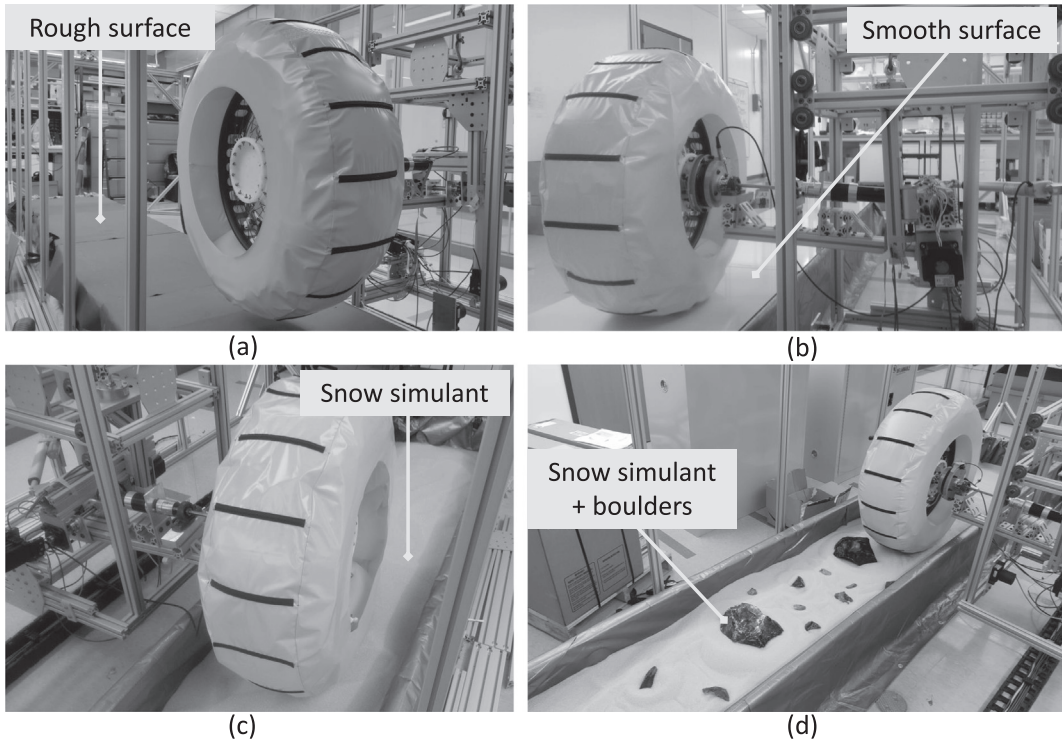


Fig. 12. Re-configurable simulants which can simulate a wide range of surfaces which might be encountered on Ocean Worlds. (a) Flat rough surface created using sandpaper laid on top of a polycarbonate panel. (b) Flat smooth surface created using a polycarbonate panel. (c) Snow simulant created using fine glass bubbles. (d) Simulated snow and ice boulder field.

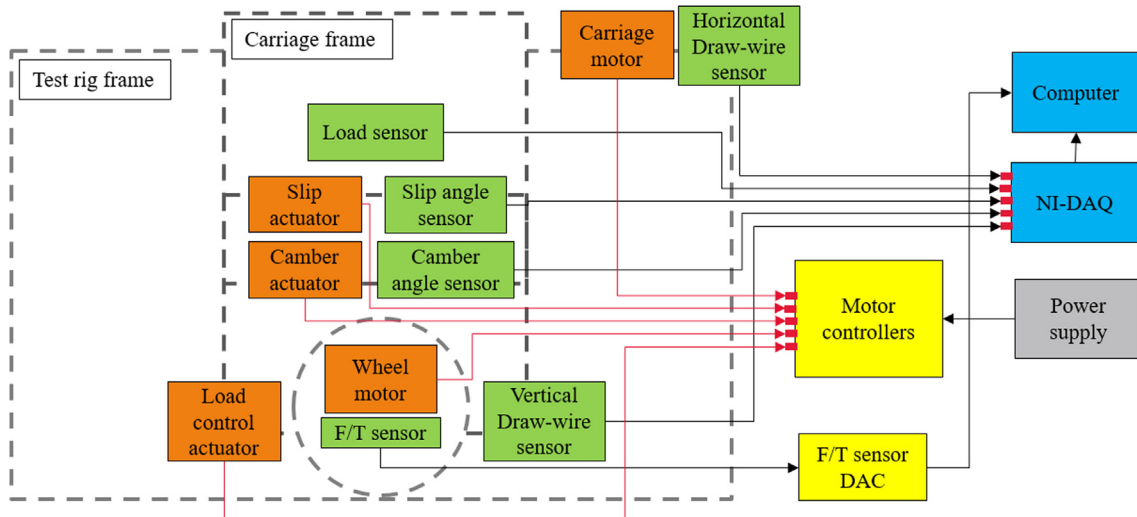


Fig. 13. Electrical and control system layout. The green blocks are sensors. The yellow blocks are motors or actuators. The orange blocks indicate controllers.

active load control. Considering the weight of the drive, vertical motion, and camber and slip structures, the load cell used is the FUTEK LCF450 which can measure up to 1300 N. Two draw-wire sensors are used to measure the horizontal carriage displacement and vertical wheel displacement. The horizontal carriage system uses the Micro-Epsilon WDS-P115 sensor with a measuring range of up to 7.5 m. The vertical wheel displacement is measured using a Micro-Epsilon WPS-MK88 sensor with a measuring range of 2.3 m. The vertical draw-wire sensor provides measurement of the wheel sinkage and deformation over different surface features. The slip angle is measured using a P3 America ERCF 1 rotary encoder and the camber angle is measured using a TTI Americas

G-NSDOG2-003 inclinometer. The carriage motor and the wheel drive motor have their own integrated encoders which are used to control the carriage horizontal speed and the wheel RPM.

3.4. Software interface

The FT sensor and the National Instrument data acquisition I/O device (which interfaces all of the other sensors and actuators) are directly wired to the desktop machine via USB. The test rig operator interfaces with these systems using the LabVIEW software package. The FT sensor comes pre-packaged with a LabVIEW program to obtain the raw voltage inputs and convert these values

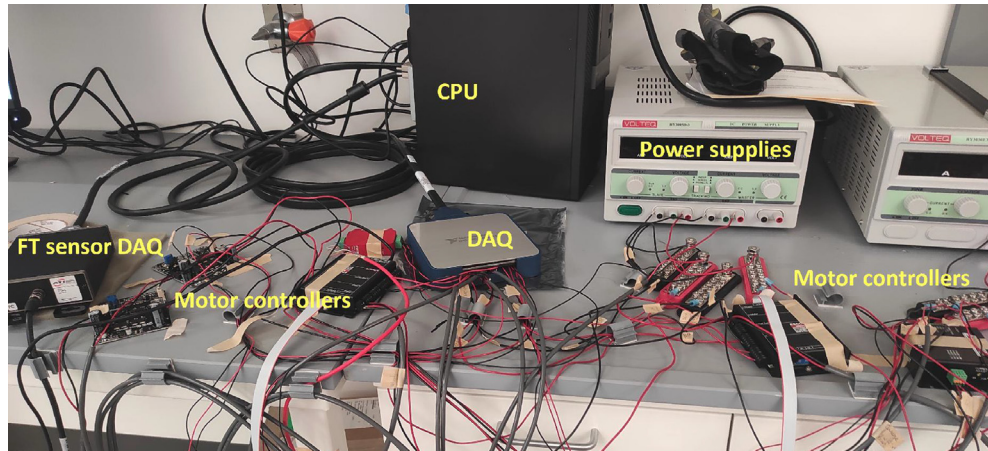


Fig. 14. Electrical components for motor control and sensor data acquisition.



Fig. 15. Energy chain routing the wires from the moving carriage to the electrical components on the table. Right: close-up view showing the cables inside the energy chain.

into the 3-axis forces and torques, using a manufacturer-provided calibration matrix. This program comes with the built-in functionality to record data at the desired sample rate that is then written to a CSV file. The base program is further enhanced to facilitate the simultaneous recording of all other sensor data from the data acquisition system in addition to the primary data collection from the FT sensor. The enhanced program allows the operator to view both the raw and calibrated data from all sensors connected to the primary data acquisition system in addition to the force and torque data, and when data collection starts all of the sensor data is recorded, as shown in Fig. 16. In addition to the data collection program, several other LabVIEW programs are used to control the different actuators and motors, as shown in Fig. 17. Prior to beginning a test, these programs allow the operator to set a desired vertical load, horizontal speed, slip ratio, slip angle, and camber angle. The wheel is run for the entire available length of the test bed, after which the wheel is raised and the carriage moved back to the starting position for the next test run. At the end of each test run, the collected data from all sensors is written to various CSV files.

4. Prototype wheel fabrication

All Mars rovers to date have used wheels that are rigid and relatively small, primarily due to volume constraints (Skonieczny et al., 2012). Compared to small-diameter wheels, large wheels can offer superior performance in traversing large obstacles such as boulders. Small-diameter wheels are more likely to experience sinkage in loose soil compared to larger wheels since they have reduced surface contact area and also permanent wheel damage

when traversing sharp rock formations. Fig. 18(a) shows the damage to the aluminum wheel ($D = 0.50$ m) of the Curiosity rover on Mars after traversing an area with ventifacts (sharp wind-eroded rock formations cemented into the ground) (Toupet et al., 2018). Fig. 18(b) shows the modified wheel design for the Perseverance rover, with a slightly larger diameter and a different grouser pattern to improve its performance (Inotsume et al., 2019). The joint NASA-ESA Mars Sample Return (MSR) mission rover has currently baselined a compliant wheel using shape memory alloy as shown in Fig. 18 (c) which can conform to sharp and irregular surfaces, providing excellent traction and without sustaining damage (Muirhead et al., 2020). Rovers sent to Ocean Worlds such as Europa will likely encounter much more jagged terrain and sharp ice and rock formations than seen on Mars (Nayar et al., 2019). This section details the design and construction of the prototype of a novel deployable and compliant large-diameter wheel design which can be stowed during launch and cruise, and is well suited for extreme terrain mobility.

4.1. Wheel requirements

The extremely cold environment the rover will operate in, the potentially rugged terrain and largely unknown surface material properties have led to the following requirements for the Ocean World rover wheel prototype. The wheel shall be capable of overcoming an obstacle 0.5 meters in height. The size of obstacles that a rover can surmount is primarily a function of the vehicle suspension system and the wheel diameter. The rocker-bogie design used by the Mars rovers allows the rover to go over obstacles that are up

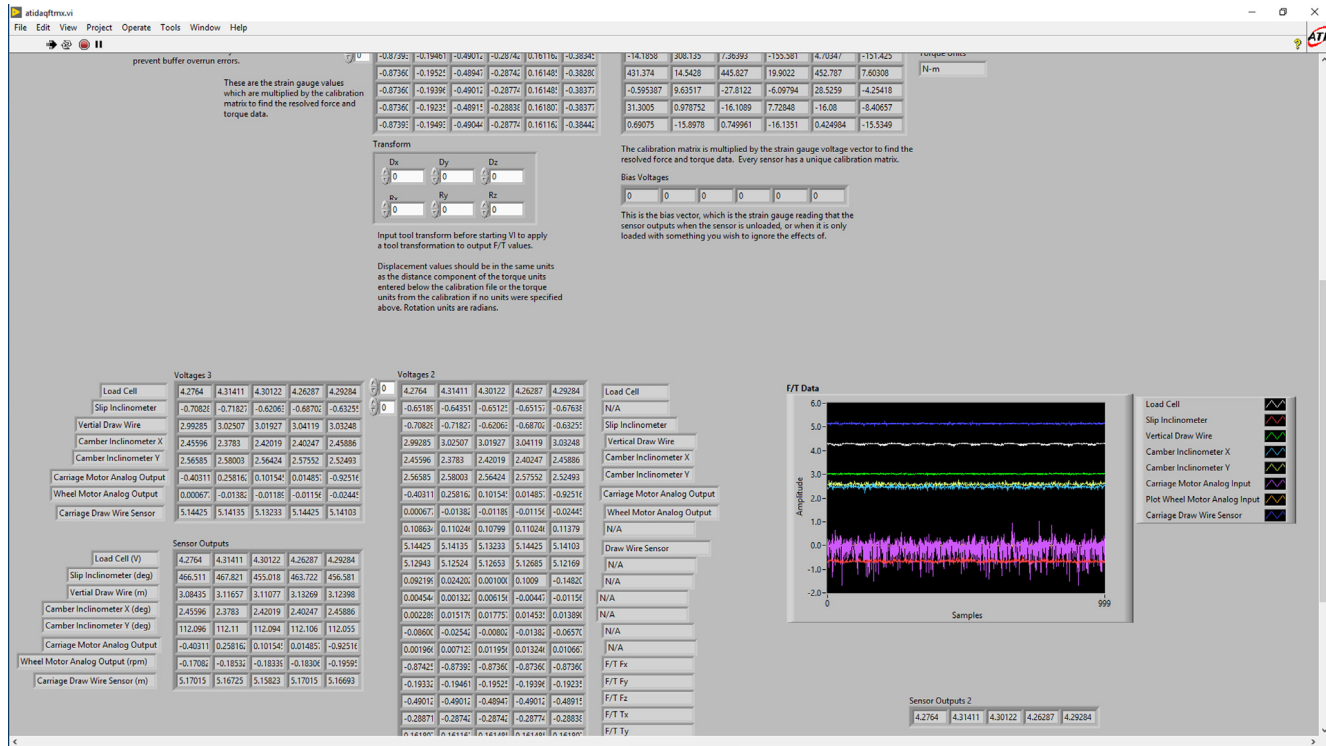


Fig. 16. LabVIEW program that allows for the viewing and recording of all sensor data.

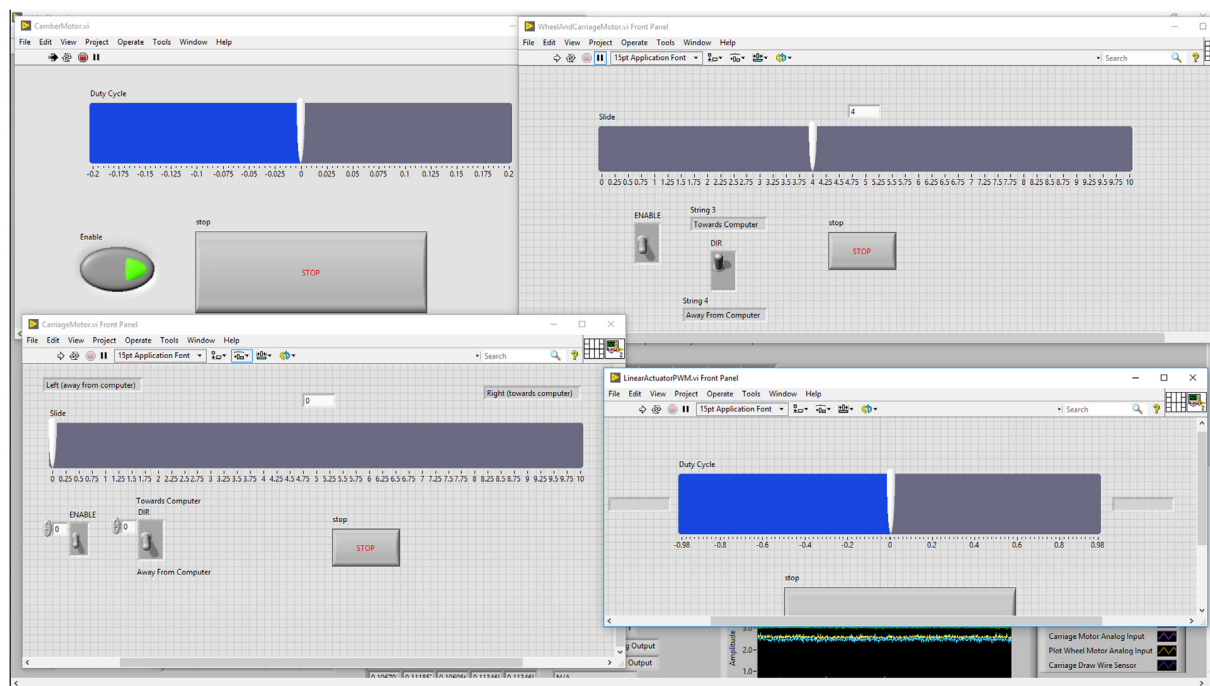


Fig. 17. LabVIEW programs to allow the operator to control the carriage horizontal speed and direction, wheel RPM and direction, slip angle, and camber angle.

to about 1.5 to 2 times the wheel diameter. However, the rocker-bogie suspension system is mechanically complex, limits the traverse speed, and presents challenges in extremely cold environments where the actuators must be kept warm and lubricated. This study proposes to use a mechanically simpler four-wheel drive vehicle such as that used by the Lunar Roving Vehicle where all moving parts can be housed inside the main chassis, and hence

avoid problems with lubrication in extremely cold environments. However, such vehicles can only overcome obstacles that are about half the diameter of the wheels. To make up for this limitation of the four-wheel design, it is proposed to use large-diameter wheels (> 1 meter) to overcome obstacles up to 0.5 m. Large-diameter wheels present inherent difficulty for packaging onboard the delivery spacecraft, aeroshell, and launch vehicle fairing due to volume



Fig. 18. Left to right: (a) Damage on the rigid Curiosity rover wheels. (b) Mars 2020 rover wheel with modified grouser pattern. (c) Compliant shape memory alloy wheel baselined for the MSR sample fetch rover undergoing obstacle tests at NASA Glenn Research Center.

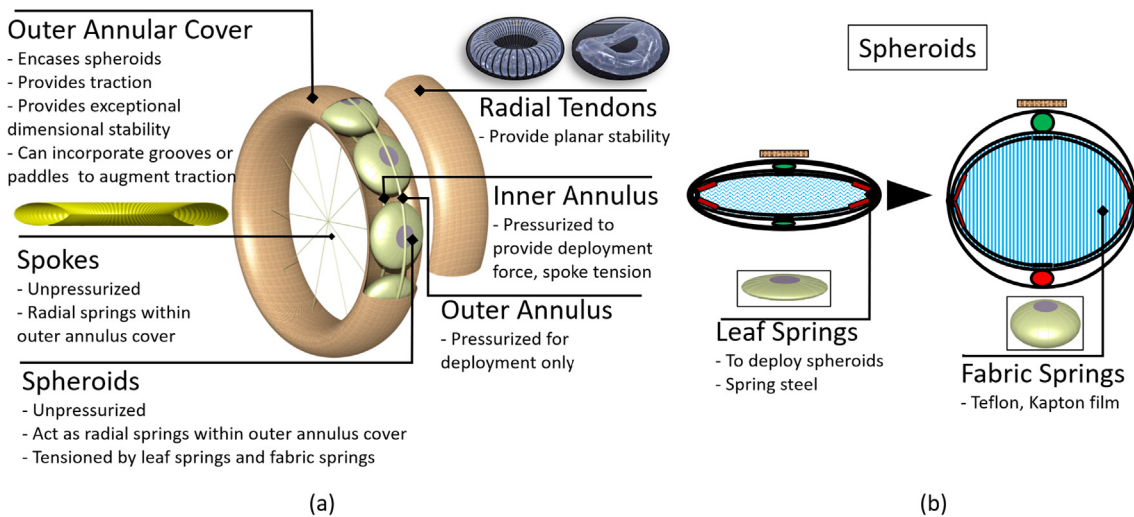


Fig. 19. Conceptual design of the large diameter deployable tire for Ocean World rover. (a) Components of the tire assembly. (b) Cross-section of spheroids.

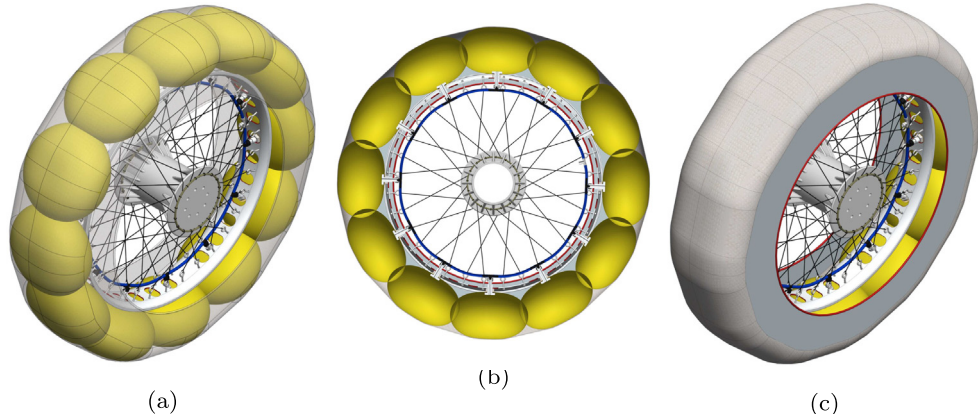


Fig. 20. Design rendering of the prototype wheel. (a) Spheroids inside an exterior cover form the tire portion of the wheel and are mounted on a circular metallic ring which is, in turn, connected to the central wheel hub with an array of braided fiber "spokes". (b) Axial view of the tire interior. (c) Tire with the exterior cover.

constraints. The proposed wheel design will be stowed in a compact configuration during launch and cruise, and will be deployed to its final configuration just before touchdown during the sky crane maneuver. Compared to rigid tires used on the Mars rovers, the proposed tire will conform to the surface features. This allows

greater contact surface area and better traction on irregular surfaces and reduces the risk of wheel damage from sharp rock and ice formations. The design should allow scaling and performance prediction for potentially larger diameter deployable tires (> 5 m) which may be required depending on the conditions at the

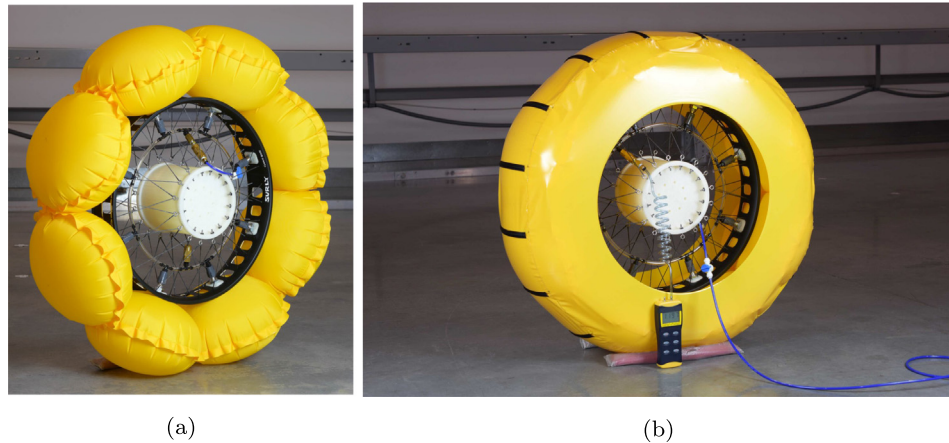


Fig. 21. Fabricated prototype wheel. (a) 8 inflated UHPV spheroids on a black metallic rim and tensioned, braided fiber "spokes". (b) Exterior cover installed over the UHPV segments.

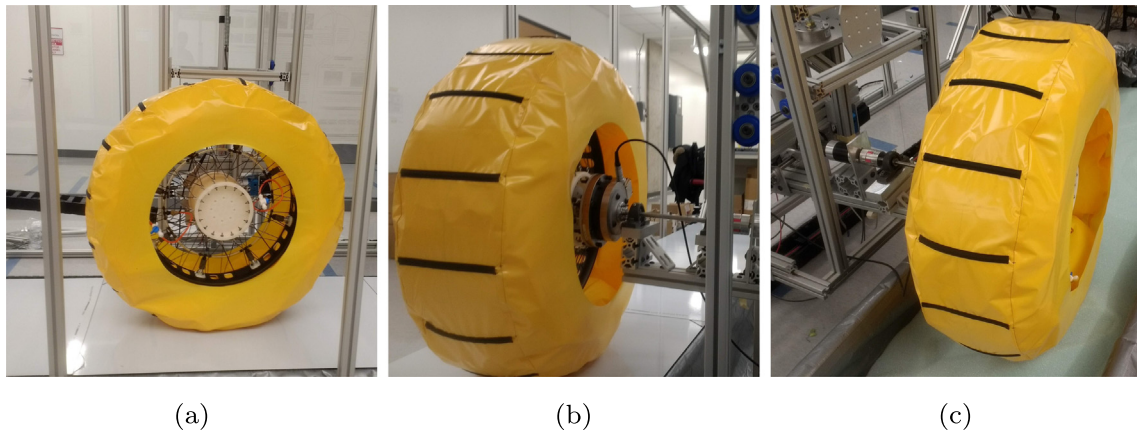


Fig. 22. Prototype tire mounted on test rig. (a) Front view of the inflated tire sitting on a smooth surface. (b) Back view showing the wheel hub assembly attached to the test rig assembly. (c) Side view showing the tire mounted and resting in the surface simulant box.

landing site and science operations area. The wheel must be made of materials that are wear-resistant to sharp surface features, under extremely cold temperatures, and must be resistant to radiation from energetic charged particles on Europa's surface.

4.2. Wheel design concept

The intent in the design of the test tire is twofold: 1) To support the development and validation of a single-wheel test rig, and 2) To incorporate basic attributes that are functionally relevant to the Ocean World application. The test wheel developed by Thin Red Line Aerospace (TRLA) is based on a cutting-edge fabric structure called Ultra High Performance Vessel (UHPV). UHPV was developed by TRLA to address NASA's problem with performance predictability in inflatable structures. TRLA has participated in numerous NASA programs developing mission applications of its patented fabric architecture and validating the predictable scalable performance of its unique structures ([de Jong, 2010a; de Jong, 2010b; de Jong, 2009](#)).

The conceptual design for Ocean World application, as shown in [Fig. 19](#), is created by combined utilization of UHPV annulus and oblate spheroid geometries. The exterior tire surface is an unpressurized annulus vessel that is tensioned by a series of interior UHPV oblate spheroids. The configuration is similar to that of ball bearings in a race. The spheroids are also unpressurized, and their radial tendons are tensioned by embedded leaf springs that force

the default geometry into place. In addition, a pair of narrow annulus vessels are located within the tire assembly along a circumferential path above and below the spheroids. The narrow annulus vessels are pressurized during the deployment process to expand the fabric assembly into its functional geometry. Once deployed, the leaf springs in the oblate spheroids lockup, and the tire assembly does not require the outer narrow annulus to be pressurized. However, the smaller diameter inner annulus is required to be pressurized to keep the spokes that form the wheel to be tensioned. This inner annulus is well distanced from the tire tread that remains in contact with the surface. The reliability of the tire can be greatly increased by providing a redundant inner annulus at a very small increase in cost. The resultant configuration is extremely resistant to puncture. In the scenario where sharp rocks penetrate the outer annulus, outer cover, or interior spheroids, the tire remains intact since these parts do not have to be pressurized once deployed. The only critical pressurized part is the inner annulus and it is separated from the surface by the spheroids and outer annulus. Additionally, the lightweight and rugged tire design conforms to rocky and jagged surfaces which eliminates concentrated contact loads on the tire. The small diameter rigid wheels used on Mars rovers have reduced surface contact area, making them relatively more prone to damage by sharp rocks. The conformable shape memory alloy wheels provide similar benefits to the proposed deployable wheel, however, are much heavier for large diameter requirements and pose packaging challenges. The inflat-

Table 2

Test cases with prototype wheel.

Test #	Load, N	Slip ratio	Slip angle, deg.	Camber, deg.	Surface
1	10	0	0	0	Sandpaper
2	20	0	0	0	Sandpaper
3	30	0	0	0	Sandpaper
4	40	0	0	0	Sandpaper
5	50	0	0	0	Sandpaper
6	10	0.1	0	0	Sandpaper
7	20	0.1	0	0	Sandpaper
8	30	0.1	0	0	Sandpaper
9	40	0.1	0	0	Sandpaper
10	50	0.1	0	0	Sandpaper
11	10	0.2	0	0	Sandpaper
12	20	0.2	0	0	Sandpaper
13	30	0.2	0	0	Sandpaper
14	40	0.2	0	0	Sandpaper
15	50	0.2	0	0	Sandpaper
16	10	0.3	0	0	Sandpaper
17	20	0.3	0	0	Sandpaper
18	30	0.3	0	0	Sandpaper
19	40	0.3	0	0	Sandpaper
20	50	0.3	0	0	Sandpaper
21	10	0.4	0	0	Sandpaper
22	20	0.4	0	0	Sandpaper
23	30	0.4	0	0	Sandpaper
24	40	0.4	0	0	Sandpaper
25	50	0.4	0	0	Sandpaper
26	10	0.5	0	0	Sandpaper
27	20	0.5	0	0	Sandpaper
28	30	0.5	0	0	Sandpaper
29	40	0.5	0	0	Sandpaper
30	50	0.5	0	0	Sandpaper
31	10	0.6	0	0	Sandpaper
32	20	0.6	0	0	Sandpaper
33	10	0.7	0	0	Sandpaper
34	60	0	0	0	Sandpaper
35	60	0.1	0	0	Sandpaper
36	70	0.1	0	0	Sandpaper
37	10	0	0	0	Glass beads
38	70	0	0	0	Glass Beads
39	50	0	0	0	Glass beads
39	50	0	0	0	Glass beads
40	70	0	0	0	Glass beads
41	10	0.1	0	0	Glass beads
42	30	0.2	0	0	Glass beads
43	50	0.2	0	0	Glass beads
44	70	0.2	0	0	Glass beads
45	30	0.2	0	0	Glass beads
46	30	0.3	0	0	Glass beads
47	30	0.4	0	0	Glass beads
48	30	0.5	0	0	Glass beads
49	50	0.3	0	0	Glass beads
50	50	0.5	0	0	Glass beads
51	50	0.7	0	0	Glass beads
52	10	0	0	0	Sandpaper
53	20	0	0	0	Sandpaper
54	30	0	0	0	Sandpaper
55	40	0	0	0	Sandpaper
56	50	0	0	0	Sandpaper
57	10	0	10	0	Sandpaper
58	20	0	10	0	Sandpaper
59	30	0	10	0	Sandpaper
60	40	0	10	0	Sandpaper
61	50	0	10	0	Sandpaper
62	10	0	20	0	Sandpaper

able tire is a lightweight, rugged tire design that conforms to rocky and jagged surfaces which eliminate concentrated contact loads on the tire. The tire can be compactly stowed during launch and will be deployed just prior to landing. The UHPV fabric structure makes the design scalable to larger diameters.

In the prototype wheel, the geometry defined in the conceptual design is created using inflatable UHPV oblate spheroids. These spheroids are installed on a metallic rim. An exterior cover is

installed to create the effect of the outer annulus cover by enhancing the circularity of the tire's outer mold line. Fig. 20 shows a rendering of the prototype design.

The fabricated prototype wheel is shown in Fig. 21. There are eight inflatable UHPV segments mounted around the outside circumference of a black metallic wheel rim. A central wheel hub facilitates the attachment of the wheel assembly to the test rig's axle. Structural concentricity of the hub and the rim is provided

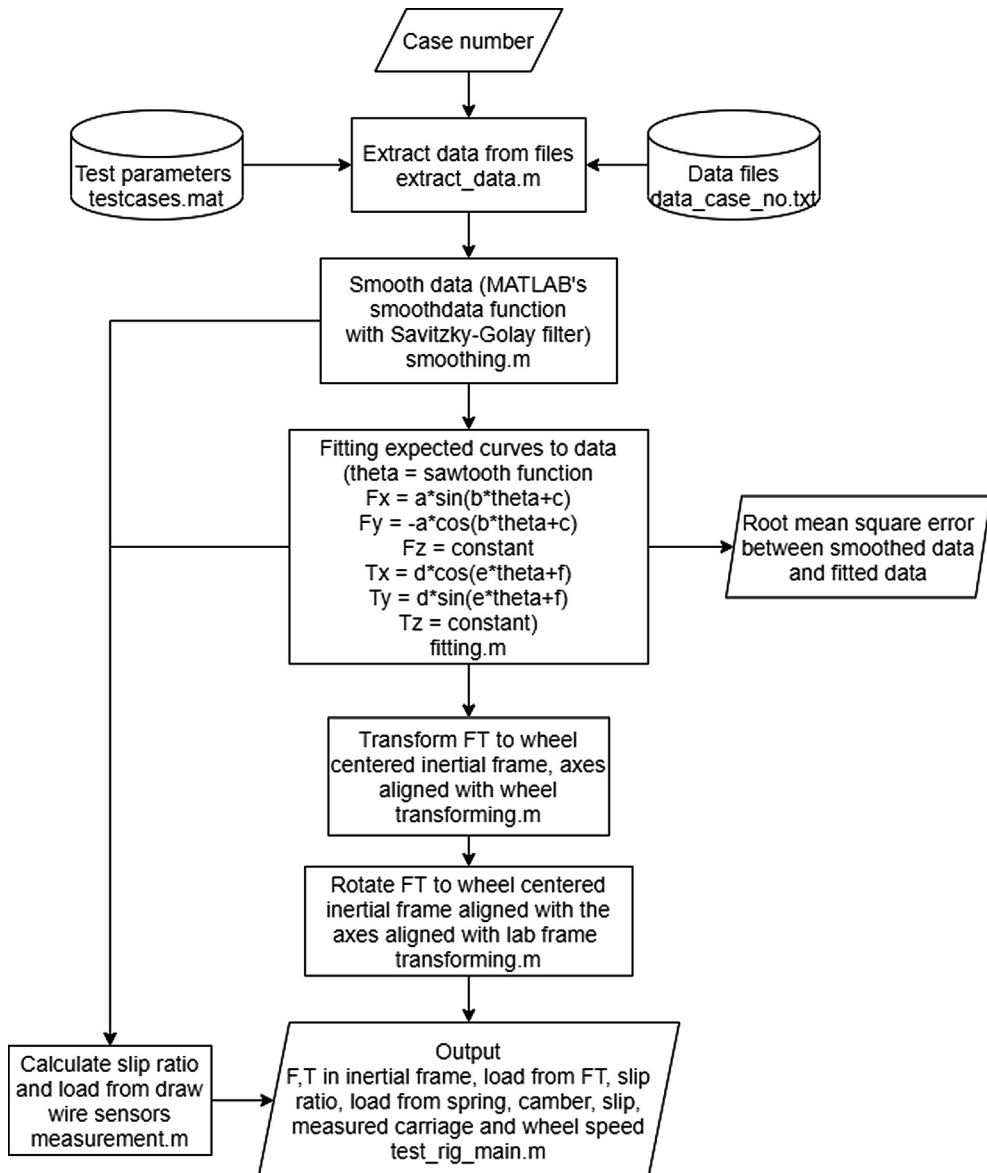


Fig. 23. Data processing algorithm for analysis of sensor data.

by an array of 64 flexible Vectran® fiber cordage tendon spokes. An exterior cover is installed over the eight UHPV inflatable segments. The cover reacts to the axial distension of the UHPV inflatables (i.e., radially outwards from the center) to enhance the circularity of the tire's outer mold line. All eight yellow inflatable UHPV tire segments are pneumatically manifolded to one another by means of a circle of clear plastic tubing concentrically positioned between the wheel rim and hub. The tread surface of the tire incorporates sixteen sleeves into which tubing stiffeners are inserted to simulate tread-like protrusions.

4.3. Integration with test rig

The tire is mounted on the test rig by attaching the wheel hub to the axle of the wheel motor on the rig. Fig. 22 shows the mounted tire. A shaft collar is attached to the end of the wheel motor axle. The FT sensor is fitted with adapters on both sides. One end is attached to the shaft collar and the other to the wheel hub. The adapter between the sensor and wheel hub can be modified to mount different wheels. The tire can roll in the surface simulant box along the length of the test rig. The entire wheel drive

axle can be tilted along two axes to achieve non-zero slip and camber angles.

5. Test results with prototype wheel

To demonstrate the capability of the test rig, a number of tests were performed with various vertical loads, slip ratios, slip angles, and surfaces. Table 2 lists the tests performed in this study. The LabVIEW interface is used to set the parameters, start the test, and record all sensor data at the end of each test. A set of experiments were performed at an independent facility to validate the measurements from the single wheel test rig. However, due to limitations of achievable vertical load in the two test rigs the data could not directly be compared and hence the validation exercise could not be completed.

5.1. Data analysis

The data analysis process consists of filtering, smoothing, and fitting the sensor data to sinusoidal curves to extract the drawbar pull force, lateral force, and driving torque. Fig. 23 shows an over-

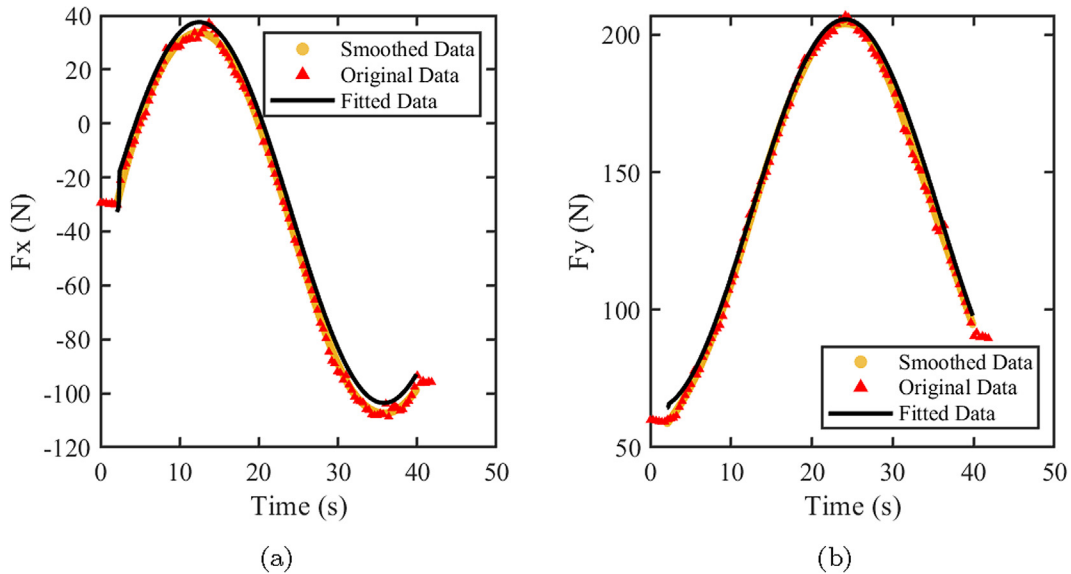


Fig. 24. Data fits for F_x and F_y in the wheel rotating frame.

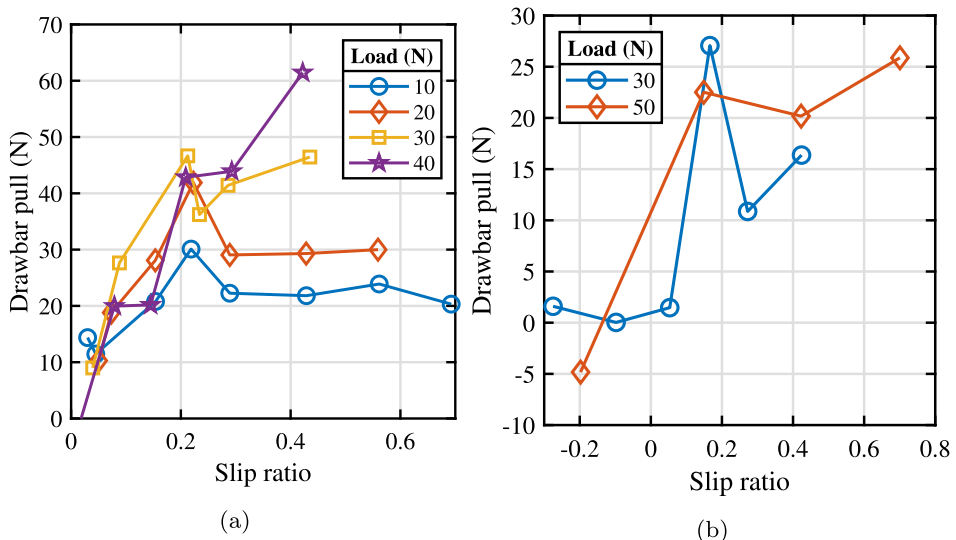


Fig. 25. Draw bar pull force vs slip ratio for various vertical loads. (a) On flat rough surface. (b) On glass beads snow simulant.

view of the data-processing algorithm. The sensor data along with the parameters of a single test are recorded in a file. The input parameters for a test include load, slip ratio, slip angle, and camber angle. The data corresponding to the FT sensor, load cell, vertical and horizontal draw wire sensor, inclinometer, and rotary sensor is extracted.

A filter is applied to smooth the raw FT sensor data and then a sinusoidal curve is fitted. The root mean square error for each fit is calculated to measure the accuracy of the fit. The FT sensor is fixed on the wheel and thus gives output in the rotating frame. The FT sensor data is transformed to obtain the measurements in the fixed inertial frame. Fig. 24 shows plots for FT sensor output data along with the smoothed and fitted data points for F_x and F_y , for the case of 10 N load, zero slip ratio, zero slip and camber angles. A sine and cosine function is fitted for F_x and F_y respectively. The ideal fitted curves agree well with the original data. The curves have a constant bias that is eliminated when transforming into the inertial frame. The fitting error for the drawbar pull force was calculated as the root mean square error (RMSE), normalized using the fitted

drawbar pull value for a given test case. About 65% of the data has an RMSE of less than 0.2 (20% of measured drawbar pull force value) and 80% has an RMSE of less than 0.3.

5.2. Test results and discussion

All tests were performed on the prototype wheel with two surfaces: (1) flat surface with sand paper, and (2) ocean worlds surface simulant - glass beads. Fig. 25 shows drawbar pull force as a function of slip ratio for various vertical loads. The drawbar pull force or traction force rapidly increases with increasing slip ratio, up to about 0.2. Beyond slip ratio of 0.2, the drawbar pull increases only slightly. The drawbar pull also increases with increasing vertical loads. These trends are qualitatively consistent with results from experimental tests and numerical simulations in the literature (Chunlai and Mengyan, 2015; Yang et al., 2016; Mousavi and Sandu, 2020; Yoshida et al., 2010; Zang and Zhao, 2013).

Fig. 26(a) shows the variation of resistance torque about the wheel rotating axis with slip ratio for various vertical loads. As

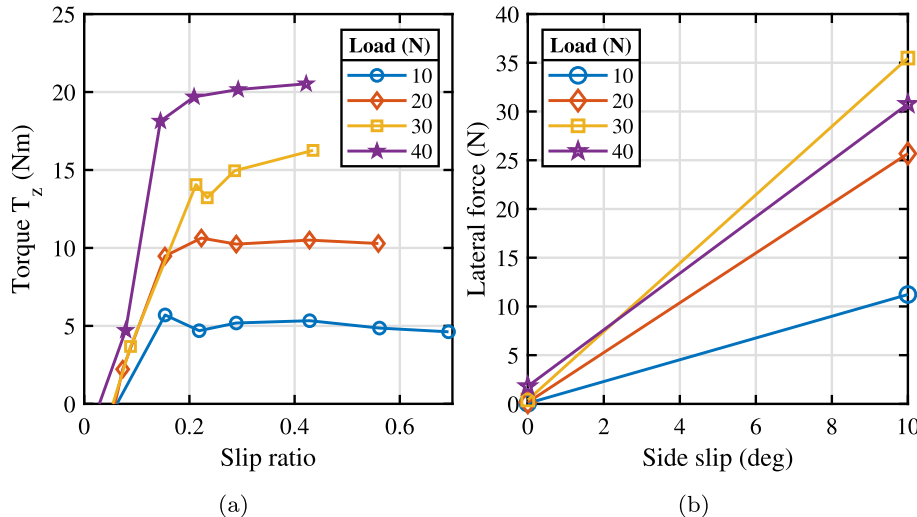


Fig. 26. (a) Torque vs slip ratio for various loads on a flat rough surface. (b) Lateral force vs side slip angle for various vertical loads on a flat rough surface. The slip ratio is zero.

with the drawbar pull, the torque increases sharply till the slip ratio reaches about 0.2 beyond which it flattens out. The torque also increases with increasing load, as expected. These trends are also in qualitative agreement with results in the literature (Liu et al., 2008; Kim and Yu, 2020). Fig. 26(b) shows the lateral force as a function of slip angle for two vertical loads. The small non-zero values are due to asymmetry in the actual wheel and a very small non-zero slip angle due to step control of the motors. The non-zero large lateral force for a 10° slip angle is expected since the wheel rotation axis and direction of traverse are not perpendicular, so the traction force has a component in the axis perpendicular to the traverse direction.

These preliminary tests demonstrate the functioning of the test rig in terms of setting the desired load, slip and camber angles, and slip ratio, measuring the forces, and data processing. More tests are required to test endurance and repeatability and to perform statistical analysis. An extensive testing campaign will be required to better quantify the performance of the test rig.

6. Conclusions

The present work described the design, construction, and initial test results from a novel single wheel test rig for Ocean World rovers. The test rig allows independent control of the slip ratio, vertical load, slip angle, and camber angle and accommodates large-diameter deployable wheels. The test rig has been built using commercially available mechanical parts and electrical actuators. The modular simulant bed allows for a wide range of surfaces to be simulated including flat smooth and rough surfaces, snow, and rock-ice boulder fields. The forces and moments on the wheel, wheel sinkage, and wheel torque are measured by commercial sensors. A 1-meter diameter prototype wheel that incorporates the basic functionality of the proposed large-diameter rover wheel has been fabricated and tested. Preliminary results of the drawbar pull, driving torque, and lateral force with the test wheel as a function of slip ratio, vertical load, and slip angle are consistent with those in the literature and demonstrate the basic functionality of the new single wheel Ocean World test rig. Further testing is required for a complete statistical analysis of the test rig and the tire.

Declaration of Competing Interest

The authors declare that they have no known competing financial interests or personal relationships that could have appeared to influence the work reported in this paper.

Acknowledgments

This work was supported by the NASA Planetary Science Division under the Concepts for Ocean Worlds Life Detection Technology (COLDTech) program (NNH16ZDA001N). We acknowledge Jithin Prabha at Purdue University and the supportive staff at the Purdue Bechtel Innovation Design Center for their assistance in the fabrication of various test rig components. We also acknowledge Dr. David Kish and Reid Schmidt, both at the Purdue FLEX Lab for their support and assistance with building facilities during the entire project.

References

- Arvidson, R.E., 2014. Roving on mars with opportunity and curiosity: terramechanics and terrain properties. *Earth Space* 2014, 165–173. [https://doi.org/10.1061\(9780784479179.019](https://doi.org/10.1061(9780784479179.019).
- Arvidson, R., DeGrosse Jr, P., Grotzinger, J., Heverly, M., Shechet, J., Moreland, S., Newby, M., Stein, N., Steffy, A., Zhou, F., et al., 2017. Relating geologic units and mobility system kinematics contributing to Curiosity wheel damage at Gale Crater, Mars. *J. Terramech.* 73, 73–93. <https://doi.org/10.1016/j.jterra.2017.03.001>.
- Arvidson, R.E., Ashley, J.W., Bell, J., Chojnacki, M., Cohen, J., Economou, T., Farrand, W.H., Ferguson, R., Fleischer, I., Geissler, P., et al., 2021. Opportunity Mars Rover mission: Overview and selected results from Purgatory ripple to traverses to Endeavour crater. *J. Geophys. Res.: Planets* 116 (E7). <https://doi.org/10.1029/2010JE003746>.
- Balaran, B., Canham, T., Duncan, C., Grip, H.F., Johnson, W., Maki, J., Quon, A., Stern, R., Zhu, D., 2018. Mars Helicopter Technology Demonstrator. In: 2018 AIAA Atmospheric Flight Mechanics Conference, Kissimmee, FL, p. 0023. <https://doi.org/10.2514/6.2018-0023>.
- Barnes, J.W., Turtle, E.P., Trainer, M.G., Lorenz, R.D., MacKenzie, S.M., Brinckerhoff, W.B., Cable, M.L., Ernst, C.M., Freissinet, C., Hand, K.P., et al., 2021. Science goals and objectives for the dragonfly titan rotorcraft relocatable lander. *Planet. Sci. J.* 2 (4), 130. <https://doi.org/10.3847/PSJ/abfdcf>.
- Chunlai, Z., Mengyan, Z., 2015. Simulation of tire-sand interactions based on FEM/ DEM. *J. South China Univ. Technol.: Nat. Sci. Ed.* 43 (8), 75–81. <https://doi.org/10.1016/j.jterra.2014.05.005>.
- de Jong, M., 2009. Advanced Inflatable Radiation Shielding, NASA Phase I SBIR Report, Tech. Rep. X4.01-8801, NASA Langley Research Center.
- de Jong, M., 2010. Integrated Inflatable Ballute for Planetary Entry, NASA Phase II SBIR Report, Tech. Rep. X9.02-9443, NASA Ames Research Center.

- de Jong, M., 2010. Verification and Validation of Innovative Inflatable Structures Design, NASA Phase II SBIR Report, Tech. Rep. X4.02-9770, NASA Langley Research Center.
- Ding, L., Deng, Z., Gao, H., Nagatani, K., Yoshida, K., 2011. Planetary rovers' wheel-soil interaction mechanics: new challenges and applications for wheeled mobile robots. *Intel. Serv. Robot.* 4 (1), 17–38. <https://doi.org/10.1007/s11370-010-0080-5>.
- Ding, L., Deng, Z., Gao, H., Guo, J., Zhang, D., Iagnemma, K.D., 2013. Experimental study and analysis of the wheels' steering mechanics for planetary exploration wheeled mobile robots moving on deformable terrain. *Int. J. Robot. Res.* 32 (6), 712–743. <https://doi.org/10.1177/0278364912468357>.
- Ellery, A., 2016. Survey of Past Rover Missions. Springer Science & Business Media. https://doi.org/10.1007/978-3-642-03259-2_3.
- Fiorini, P., Hayati, S., Heverly, M., Gensler, J., 1999. A hopping robot for planetary exploration. In: 1999 IEEE Aerospace Conference, Vol. 2, IEEE, Aspen, CO, pp. 153–158. <https://doi.org/10.1109/AERO.1999.793156>.
- Gallina, A., Krenn, R., Scharringenhausen, M., Uhl, T., Schäfer, B., 2014. Parameter identification of a planetary rover wheel-soil contact model via a Bayesian approach. *J. Field Robot.* 31 (1), 161–175. <https://doi.org/10.1002/rob.21480>.
- Genta, G., Pizzamiglio, C., 2016. Testing of planetary rover wheels: Design and setup of a testing machine. In: 2016 IEEE Metrology for Aerospace (MetroAeroSpace), IEEE, Florence, Italy, pp. 43–48. <https://doi.org/10.1109/MetroAeroSpace.2016.7573183>.
- Hand, K., Murray, A., Garvin, J., Brinckerhoff, W., Christner, B., Edgett, K., Hoehler, T., et al., 2017. Report of the Europa Lander Science Definition Team, Tech. Rep. JPL D-97667, Washington D.C. URL <https://europa.nasa.gov/resources/58/europa-lander-study-2016-report>.
- Hand, K.P., Phillips, C.B., Murray, A., Garvin, J., Maize, E., Gibbs, R., Reeves, G., San Martin, A., Tan-Wang, G., Krajewski, J., et al., 2022. Science goals and mission architecture of the europa lander mission concept. *Planet. Sci. J.* 3 (1), 22. <https://doi.org/10.3847/PSJ/ac4493>.
- Hassanalian, M., Rice, D., Abdelkefi, A., 2018. Evolution of space drones for planetary exploration: A review. *Prog. Aerosp. Sci.* 97, 61–105. <https://doi.org/10.1016/j.paerosci.2018.01.003>.
- Henderson, B.L., Gudipati, M.S., Bateman, F.B., 2019. Leeb hardness of salty Europa ice analogs exposed to high-energy electrons. *Icarus* 322, 114–120. <https://doi.org/10.1016/j.icarus.2019.01.006>.
- Hobley, D., Moore, J., Howard, A., 2013. How Rough is the Surface of Europa at Lander Scale? In: 44th Lunar and Planetary Science Conference, The Woodlands, TX, p. 2432. URL <https://www.lpi.usra.edu/meetings/lpsc2013/pdf/2432.pdf>.
- Hobley, D.E., Moore, J.M., Howard, A.D., Umurhan, O.M., 2018. Formation of metre-scale bladed roughness on Europa's surface by ablation of ice. *Nat. Geosci.* 11 (12), 901–904. <https://doi.org/10.1038/s41561-018-0235-0>.
- Iagnemma, K., Dubowsky, S., 2004. Mobile Robots in Rough Terrain: Estimation, Motion Planning, and Control with Application to Planetary Rovers. Springer Science & Business Media. <https://doi.org/10.1007/b94718>.
- Inotsume, H., Moreland, S., Skonieczny, K., Wettergreen, D., 2019. Parametric study and design guidelines for rigid wheels for planetary rovers. *J. Terramech.* 85, 39–57. <https://doi.org/10.1016/j.jterra.2019.06.002>.
- Ishigami, G., 2008. Terramechanics-based analysis and control for lunar/planetary exploration robots Ph.D. thesis, Tohoku University, Sendai, Japan.
- Ishigami, G., Miwa, A., Nagatani, K., Yoshida, K., 2007. Terramechanics-based model for steering maneuver of planetary exploration rovers on loose soil. *J. Field Robot.* 24 (3), 233–250. <https://doi.org/10.1002/rob.20187>.
- Kassel, S., 1971. Lunokhod-1 Soviet Lunar Surface Vehicle, Tech. Rep. R-802-ARPA, RAND Corporation, Santa Monica, CA. URL <https://apps.dtic.mil/sti/pdfs/AD0733960.pdf>.
- Kim, K.-J., Yu, K.-H., 2020. Multidisciplinary design optimization for a solar-powered exploration rover considering the restricted power requirement. *Energies* 13 (24), 6652. <https://doi.org/10.3390/en13246652>.
- Landis, G.A., LaMarre, C., Colozza, A., 2005. Venus atmospheric exploration by solar aircraft. *Acta Astronaut.* 56 (8), 750–755. <https://doi.org/10.1016/j.actaastro.2004.12.001>.
- Li, R., Wu, B., Di, K., Angelova, A., Arvidson, R.E., Lee, I.-C., Maimone, M., Matthies, L. H., Richer, L., Sullivan, R., et al., 2008. Characterization of traverse slippage experienced by Spirit rover on Husband Hill at Gusev crater. *J. Geophys. Res.: Planets* 113 (E12). <https://doi.org/10.1029/2008JE003097>.
- Ling, Z., Jolliff, B.L., Liu, C., Qiao, L., Cao, H., Zhang, J., Fu, X., Li, B., Liu, J., 2019. A Close View of Chang'e-4 landing site and science questions to be answered by Yutu-2. In: 50th Lunar and Planetary Science Conference, Lunar and Planetary Institute, The Woodlands, TX. URL <https://www.lpi.usra.edu/meetings/lpsc2019/pdf/2330.pdf>.
- Liu, J., Gao, H., Deng, Z., 2008. Effect of straight grousers parameters on motion performance of small rigid wheel on loose sand. *Informat. Technol.* 7 (8), 1125–1132. <https://doi.org/10.3923/itj.2008.1125.1132>.
- Lorenz, R.D., Zimbelman, J.R., 2014. Moving on Sand. *Dune Worlds*. Springer, pp. 259–272. https://doi.org/10.1007/978-3-540-89725-5_22.
- Lorenz, R.D., Oleson, S.R., Colozza, A.J., Jones, R., Packard, T., Hartwig, J., Newman, J. M., Gyekenyesi, J.Z., Schmitz, P., Walsh, J., 2018. Exploring Titan's cryogenic hydrocarbon seas with boat-deployed expendable dropsondes. *Adv. Space Res.* 62 (4), 912–920. <https://doi.org/10.1016/j.asr.2018.05.030>.
- Lu, J.I., 2017. Ocean worlds exploration. *Acta Astronaut.* 131, 123–130. <https://doi.org/10.1016/j.actaastro.2016.11.017>.
- Marteau, E., 2021. Science and Technology Development for the Robotic Exploration of Mars and Ocean Worlds, Tech. Rep. CL#21-1663, Pasadena, CA. URL <https://trs.jpl.nasa.gov/handle/2014/54814>.
- Mitri, G., Coustenis, A., Fanchini, G., Hayes, A.G., less, L., Khurana, K., Lebreton, J.-P., Lopes, R.M., Lorenz, R.D., Meriggiola, R., et al., 2014. The exploration of Titan with an orbiter and a lake probe. *Planet. Space Sci.* 104, 78–92. <https://doi.org/10.1016/j.pss.2014.07.009>.
- Moores, J.E., Smith, C.L., Toigo, A.D., Guzewich, S.D., 2017. Penitentes as the origin of the bladed terrain of Tartarus Dorsa on Pluto. *Nature* 541 (7636), 188–190. <https://doi.org/10.1038/nature20779>.
- Moreland, S., Skonieczny, K., Inotsume, H., Wettergreen, D., 2012. Soil behavior of wheels with grousers for planetary rovers. In: 2012 IEEE Aerospace Conference, IEEE, Big Sky, MT, pp. 1–8. <https://doi.org/10.1109/AERO.2012.6187040>.
- Mousavi, H., Sandu, C., 2020. Experimental study of tread rubber compound effects on tire performance on ice. *SAE Int. J. Commercial Vehicles* 13 (2). <https://doi.org/10.4271/02-13-02-0006>.
- Muirhead, B.K., Nicholas, A.K., Umland, J., Sutherland, O., Vijendran, S., 2020. Mars Sample Return campaign concept status. *Acta Astronaut.* 176, 131–138. <https://doi.org/10.1016/j.actaastro.2020.06.026>.
- Nayar, H., Kim, J., Meirion-Griffith, G., Chamberlain-Simon, B., Carpenter, K., Boettcher, A., Hans, M., Wilcox, B., 2017. Surface mobility on ocean worlds. In: 2017 IEEE Aerospace Conference, IEEE, Big Sky, MT, pp. 1–10. <https://doi.org/10.1109/AERO.2017.7943900>.
- Nayar, H., Kim, J., Chamberlain-Simon, B., Carpenter, K., Hans, M., Boettcher, A., Meirion-Griffith, G., Wilcox, B., Bittner, B., 2019. Design optimization of a lightweight rocker-bogie rover for ocean worlds applications. *Int. J. Adv. Rob. Syst.* 16 (6). <https://doi.org/10.1177/1729881419885696>, 1729881419885696.
- Nelson, R.M., Boryta, M.D., Hapke, B.W., Manatt, K.S., Shkuratov, Y., Psarev, V., Vandervoort, K., Kroner, D., Nebendum, A., Vides, C.L., et al., 2018. Laboratory simulations of planetary surfaces: Understanding regolith physical properties from remote photopolarimetric observations. *Icarus* 302, 483–498. <https://doi.org/10.1016/j.icarus.2017.11.021>.
- Nimmo, F., Pappalardo, R., 2016. Ocean worlds in the outer solar system. *J. Geophys. Res.: Planets* 121 (8), 1378–1399. <https://doi.org/10.1002/2016JE005081>.
- Oleson, S.R., Lorenz, R.D., Paul, M., Hartwig, J., Walsh, J., 2018. Titan submarines: options for exploring the depths of Titan's seas. In: 2018 AIAA SPACE and Astronautics Forum and Exposition, Orlando, FL, p. 5361. <https://doi.org/10.2514/6.2018-5361>.
- Pappalardo, R., Vance, S., Bagenal, F., Bills, B., Blaney, D., Blankenship, D.D., Brinckerhoff, W., Connerney, J., Hand, K., Hoehler, T.M., et al., 2013. Science potential from a Europa lander. *Astrobiology* 13 (8), 740–773. <https://doi.org/10.1089/ast.2013.1003>.
- Patthoff, D., Meirion-Griffith, G., Phillips, C., 2018. Science on Europa and Enceladus with a Mobile Platform. In: 49th Lunar and Planetary Science Conference, The Woodlands, TX. URL <https://www.lpi.usra.edu/meetings/lpsc2018/pdf/2648.pdf>.
- Porco, C.C., Helfenstein, P., Thomas, P., Ingersoll, A., Wisdom, J., West, R., Neukum, G., Denk, T., Wagner, R., Roatsch, T., et al., 2006. Cassini observes the active south pole of Enceladus. *Science* 311 (5766), 1393–1401. <https://doi.org/10.1126/science.1123013>.
- Potter, R.S., Cammack, J.M., Braithwaite, C.H., Church, P.D., Walley, S.M., 2020. A study of the compressive mechanical properties of defect-free, porous and sintered water-ice at low and high strain rates. *Icarus* 351, 113940. <https://doi.org/10.1016/j.icarus.2020.113940>.
- Premont, A., Alexandre, P., Doroftei, I., Goffin, F., 1997. A conceptual walking vehicle for planetary exploration. *Mechatronics* 7 (3), 287–296. [https://doi.org/10.1016/S0957-4158\(96\)00043-8](https://doi.org/10.1016/S0957-4158(96)00043-8).
- Reid, W., Emanuel, B., Chamberlain-Simon, B., Karumanchi, S., Meirion-Griffith, G., 2020. Mobility mode evaluation of a wheel-on-limb rover on glacial ice analogous to Europa terrain. In: 2020 IEEE Aerospace Conference, IEEE, Big Sky, MT, pp. 1–9. <https://doi.org/10.1109/AERO47225.2020.9172805>.
- Sanguino, T.D.J.M., 2017. 50 years of rovers for planetary exploration: A retrospective review for future directions. *Robot. Auton. Syst.* 94, 172–185. <https://doi.org/10.1016/j.robot.2017.04.020>.
- Schäfer, B., Gibbesch, A., Krenn, R., Rebele, B., 2010. Planetary rover mobility simulation on soft and uneven terrain. *Vehicle Syst. Dyn.* 48 (1), 149–169. <https://doi.org/10.1080/00423110903243224>.
- Senatore, C., Stein, N., Zhou, F., Bennett, K., Arvidson, R., Trease, B., Lindemann, R., Bellutta, P., Heverly, M., Iagnemma, K., 2014. Modeling and Validation of Mobility Characteristics of the Mars Science Laboratory Curiosity Rover. In: 12th International Symposium on Artificial Intelligence, Robotics and Automation in Space (i-SAIRAS), Montreal, QC, Canada, pp. 17–19. URL http://robotics.estec.esa.int/i-SAIRAS/isairas2014/Data/Session%208a/ISAIRAS_FinalPaper_0108.pdf.
- Sherwood, B., Lunine, J., Sotin, C., Cwik, T., Naderi, F., 2018. Program options to explore ocean worlds. *Acta Astronaut.* 143, 285–296. <https://doi.org/10.1016/j.actaastro.2017.11.047>.
- Skonieczny, K., Moreland, S.J., Wettergreen, D.S., 2012. A grouser spacing equation for determining appropriate geometry of planetary rover wheels. In: 2012 IEEE/RSJ International Conference on Intelligent Robots and Systems. IEEE, Vilamoura-Algarve, Portugal, pp. 5065–5070. <https://doi.org/10.1109/IROS.2012.6386203>.
- Sreenivasulu, S., Jayalekshmi, S., 2014. Terramechanics on lunar soil simulants: A review. *Int. J. Struct. Civil Eng. Res.* 3 (2), 92–103. URL <http://www.ijscer.com/uploadfile/2015042120150421032408131.pdf>.
- Tian, H., Zhang, T., Jia, Y., Peng, S., Yan, C., 2021. Zhurong: Features and mission of China's first Mars rover. *The Innovation* 2 (3). <https://doi.org/10.1016/j.xinn.2021.100121>.

- Toupet, O., Biesiadecki, J., Rankin, A., Steffy, A., Meirion-Griffith, G., Levine, D., Schadegg, M., Maimone, M., 2018. Traction control design and integration onboard the Mars science laboratory Curiosity rover. In: 2018 IEEE Aerospace Conference, IEEE, Big Sky, MT, pp. 1–20. <https://doi.org/10.1109/AERO.2018.8396761>.
- Weiss, P., Yung, K., Ng, T., Kömle, N., Kargl, G., Kaufmann, E., 2008. Study of a thermal drill head for the exploration of subsurface planetary ice layers. *Planet. Space Sci.* 56 (9), 1280–1292. <https://doi.org/10.1016/j.pss.2008.04.004>.
- Welch, R., Limonadi, D., Manning, R., 2013. Systems engineering the curiosity rover: A retrospective. In: 2013 8th International Conference on System of Systems Engineering, IEEE, Maui, HI, pp. 70–75. <https://doi.org/10.1109/SYSoSE.2013.6575245>.
- Williford, K.H., Farley, K.A., Stack, K.M., Allwood, A.C., Beaty, D., Beegle, L.W., Bhartia, R., Brown, A.J., de la Torre Juarez, M., Hamran, S.-E., et al., 2020. The NASA Mars 2020 rover mission and the search for extraterrestrial. In: From Habitability to Life on Mars. Elsevier, pp. 275–308. <https://doi.org/10.1016/B978-0-12-809935-3.00010-4>.
- Yajima, N., Izutsu, N., Imamura, T., Abe, T., 2009. Scientific Ballooning: Technology and Applications of Exploration Balloons Floating in the Stratosphere and the Atmospheres of Other Planets. Springer Science & Business Media. <https://doi.org/10.1007/978-0-387-09727-5>.
- Yang, F., Sun, W., Lin, G., Zhang, W., 2016. Prediction of military vehicle's drawbar pull based on an improved relevance vector machine and real vehicle tests. *Sensors* 16 (3), 351. <https://doi.org/10.3390/s16030351>.
- Yoshida, K., Nagatani, K., Yusa, J., 2010. Traction performance of wheel and track for soft-soil traversal. In: International Conference on Robotics and Automation 2010 Planetary Rover Workshop, <https://ewh.ieee.org/conf/icra/2010/workshops/PlanetaryRovers/05-Yoshida-Traction/Yoshida-Traction.pdf>.
- Zang, M., Zhao, C., 2013. Numerical simulation of rigid wheel running behavior on sand terrain. APCOM & ISCM 21, 43. URL https://www.sci-en-tech.com/apcom2013/APCOM2013-Proceedings/PDF_FullPaper/1614.pdf.
- Zhou, F., Arvidson, R.E., Bennett, K., Trease, B., Lindemann, R., Bellutta, P., Iagnemma, K., Senatore, C., 2014. Simulations of mars rover traverses. *J. Field Robot.* 31 (1), 141–160. <https://doi.org/10.1002/rob.21483>.